NASA CR-152138

(NASA-CR-152138) SIMULATED PROPELLER SLIPSTREAM EFFECTS ON A SUPERCRITICAL WING (Douglas Aircraft Co., Inc.) 72 p
HC A04/MF A01 CSCL 21E G3/07

N79-25024
Unclas
27074

SIMULATED PROPELLER SLIPSTREAM EFFECTS ON A SUPERCRITICAL WING

By

H. Robert Welge and James P. Crowder

June 1978

Prepared Under Contract No. NAS2-9472

For

National Aeronautics and Space Administration

Ames Research Center
Moffett Field, California

By

Douglas Aircraft Company
McDonnell Douglas Corporation
Long Beach, California

1. Report No. NASA CR-152138	2. Government Accession No.	3. Recipient's Catalog No
4. Title and Subtitle Simulated Propeller Slipstream Effects on a Supercritical Wing		5. Report Date June 1978 6. Performing Organization Code
7. Author(s) H. Robert Welge, James P. Crowder		8. Performing Organization Report No.
9. Performing Organization Name and Address Douglas Aircraft Company McDonnell-Douglas Corporation Long Beach, California 90846		10. Work Unit No. 11. Contract or Grant No. NAS2-9472
12. Sponsoring Agency Name and Address National Aeronautics and Space Administration Ames Research Center Moffett Field, California 94035		13. Type of Report and Period Covered Contractor Report 14. Sponsoring Agency

15. Supplementary Notes: Project Managers: Daniel P. Bencze and Ronald C. Smith, Aircraft Aerodynamics Branch, NASA-Ames Research Center, Moffett Field, California 94035

16. Abstract

To quantify the installed performance of high speed (M = 0.8) turboprop propulsion systems, an experimental program designed to assess the magnitude of the aerodynamic interference of a propeller slipstream on a supercritical wing has been conducted. The test was conducted in the NASA Ames 14-Foot Wind Tunnel. An ejector-nacelle propeller slipstream simulator was used to produce a slipstream with characteristics typical of advanced propellers presently being investigated. A supercritical wing-body configuration was used to evaluate the interference effects. A traversing total pressure rake was used to make flow field measurements behind the wing and to calibrate the slipstream simulator. The force results indicated that the interference drag amounted to an increase of ten counts (ΔC_D = .0010) or about 3% of the wing-body drag for a two engine configuration at the nominal propeller operating conditions. However, at the higher swirl angles (11° vs. 7° nominally) the interference drag was favorable by about the same magnitude. Up-inboard generally was found to have less drag than up-outboard. These results were essentially independent of lift coefficient or free stream Mach number. The lift coefficient increments at a fixed angle of attack were small (≈.025) and changes to the wing surface pressures were essentially restricted to the region washed by the slipstream. The wake total pressure measurements indicated negligible effects due to power but revealed that up inboard swirl of 7° produced a low energy region on the inboard side of the slipstream.

17. Key Words (Suggested by Author(s))
Turboprop
Slipstream
Interference Drag

18. Distribution Statement
Unlimited

19. Security Classif. (of this report)	20. Security Classif. (of this page)	21. No. of Pages	22. Price*
Unclassified	Unclassified	68	

*For sale by the National Technical Information Service, Springfield, Virginia 22161

TABLE OF CONTENTS

1.0 SUMMARY

To help quantify the installed performances of high speed (M_∞ = 0.8) turbo-prop propulsions systems, an experimental program designed to assess the magnitude of the aerodynamic interference of a simulated propeller slipstream on a supercritical wing has been conducted. The test was conducted in the NASA Ames Research Center 14-Foot Wind Tunnel. An ejector-nacelle propeller slipstream simulator was used to produce propeller slipstream characteristics typical of propellers presently being investigated. A 32° swept supercritical wing-body was used to evaluate the interference effects. A traversing total pressure rake located downstream of the model was used to make flowfield measurements behind the wing and calibrate the propeller simulator. The force results indicated that interference drag effects amounted to an increase of ten counts (ΔC_D = .0010) or about three percent of the wing-body drag for a two engine configuration at the nominal propeller operating conditions. High swirl angles (0.192 rad or 11°) reduced the drag by about the same magnitude. Up-inboard swirl generally was found to have less drag than up-outboard. These results were essentially independent of airplane lift coefficient or freestream Mach number. The lift coefficient increments at a fixed angle of attack were small, about 0.025. The installation of the simulator ahead of the wing moved the wing shock forward. Changes to the wing surface pressures due to power were essentially restricted to the region washed by the slipstream. The total pressure traversing rake data indicated negligible effects due to power but revealed that up-inboard swirl of 0.122 rad (7°) produced a low energy region above the wing on the inboard side of the slipstream which may indicate some local flow separation.

2.0 INTRODUCTION

With the occurrence of fuel shortages and higher fuel prices, the emphasis on fuel conservative aircraft is increasing. Industry system studies and NASA task force studies have identified that a substantial reduction in fuel consumption is potentially available through the use of a propulsion system[1,2,3]. However, to meet passenger and airline demands it is desirable to cruise at or near current speeds, M = 0.8. Recent technology advances by Hamilton-Standard[4] have demonstrated high propeller efficiencies at these Mach numbers by use of a highly loaded, small diameter propeller called a Prop-Fan. The interference effects of the Prop-Fan slipstream on the aircraft has not been determined to date and could degrade the installed performance of the propeller-wing combination. Previously installed propulsion system performance experience using a turboprop has been limited to aircraft designed without the use of modern supercritical wing or advanced Prop-Fan technology. The need existed, therefore, to establish the technology data base for Prop-Fan installation effects on an advanced supercritical transport type wing at speeds between M = 0.7 and 0.84.

The chief source of concern regarding adverse slipstream-wing interference is due to the total pressure rise in the slipstream which produces an increased velocity downstream of the propeller. At high-speed cruise conditions the flowfield around a wing contains extensive regions of locally supersonic flow. The design of a supercritical wing concentrates on accommodating these imbedded supersonic regions in such a way as to promote a carefully controlled deceleration of the flow back to the freestream conditions with minimum losses. A characteristic of high subsonic flight speeds is that airplane economics dictate operation very close to the drag divergence Mach number. At this point the wing flowfield is very sensitive to minor changes in the onset flow. Therefore, the interaction between the slipstream and wing could result in an increase in the shock wave strength and possible boundary layer separation in the region of the wing washed by the slipstream. At the minimum this will cause an increase in the local wave drag of the wing section. Depending on the magnitude of the increase

in slipstream Mach number, the strengthened shock wave may also provoke sufficient separation to reduce the sectional lift coefficient. This would then require a compensating lift increase on the rest of the wing which would lead to a further drag increase across the entire wing. Whether the slipstream produces an increase or decrease in the local lift coefficient, there will be a span loading disturbance which will produce an increase in the induced drag as well. Increased velocity over the wing in the slipstream will also produce higher scrubbing drag due to the greater dynamic pressure in the slipstream.

The other major distinctive feature of the Prop-Fan flowfield is the swirl. This will act to induce an increase in the leading edge upwash on the upgoing side of the slipstream and a decrease on the other side. These perturbations in the wing leading edge onset flow will produce local loading changes which could aggravate already high suction peaks and result in local separations or shock waves. It is probable, however, that such adverse effects could be eliminated by careful tailoring of cambered leading edge extensions. The interaction of the wing with the slipstream swirl could result in an overall beneficial effect if the wing can recover some of the swirl energy as a local thrust.

To support ongoing system studies and identify areas for additional development it was necessary to obtain an early indication of the magnitude of these interferences. It was also desirable to separately identify the effects of increased slipstream velocity and swirl.

To accomplish this a propeller simulator was developed for use with an existing Douglas Aircraft Company wind tunnel model incorporating a wing which was designed utilizing modern supercritical wing technology. The simulator consisted of a nacelle enclosing a high pressure air driven ejector system designed to produce an accurate simulation of a typical modern Prop-Fan slipstream. By varying the simulator drive air pressure, or by changing a replaceable set of swirl vanes, a parametric variation in slipstream velocity or swirl angle was easily produced without having to develop an actual model propeller design.

In addition to the customary wing-body model force and pressure instrumentation, a computer-controlled traversing rake apparatus was utilized to survey the wing wake and to permit in-tunnel calibration of the propeller simulator.

3.0 SYMBOLS

A	area
A_D	drive nozzle primary area
AR	wing aspect ratio
A_5	ejector exit area
A_3	area of mixing section at drive nozzle location
b/2	wing semispan
c	section wing chord
C_D	drag coefficient, $DRAG/q_o S_{REF}$
c_ℓ	section lift coefficient
C_L	lift coefficient, $LIFT/q_o S_{REF}$
cm	centimeters
C_{mac}	wing mean aerodynamic chord, 19.1 cm (7.522 in)
C_P	pressure coefficient, $(P-P_o)/q_o$
C_P'	pressure coefficient corresponding to sonic velocity at the freestream total pressure.
ΔC_D*	twice the measured incremental drag with scrubbing drag removed
ΔC_L*	twice the measured incremental lift
D	diameter
D_p	propeller diameter
ft	feet
in	inches
M	Mach number
M_5	Mach number at the exit of the simulator
m	meters
Pa	pascal
P_{T_J}/P_{T_o}	peak total pressure in the slipstream divided by freestream total pressure

P_D/P_o	simulator drive pressure divided by freestream static pressure
P	static pressure
P_o	freestream static pressure
q_o	freestream dynamic pressure
r	local radius
R	outer radius
S/C	cascade (swirl vane) spacing to chord ratio
SHP	shaft horsepower
S_{REF}	wing reference area 0.2123 m^2(2.285 ft^2)
T_T	total temperature
T_{T_D}	drive nozzle total temperature
t/c	wing thickness to chord ratio
V	velocity
V_t	tangential velocity
x/c	fraction of wing local chord
y	spanwise wing location
α_{FRP}	fuselage reference plane angle of attack
α_S (or ϕ)	swirl angle, up inboard is positive
η	% of semispan
$\Lambda_{c/4}$	sweep of wing quarter chord
λ	wing taper ratio, tip chord to root chord for trapazoidal wing

SUBSCRIPTS

ave	average value
max	maximum
o	freestream or reference condition

4.0 WIND TUNNEL MODEL DESIGN AND TUNNEL INSTALLATION

The experimental equipment used for this test consisted of a supercritical wing-body model and an ejector-nacelle used to generate a simulated slipstream. The installation in the NASA Ames 14-Foot Wind Tunnel is shown in Figures 1 and 2.

The wing-body model was metric, mounted to the sting by a Task Mark XIV-A two-inch balance. The wing of the model contained 234 surface static pressures distributed chordwise at six spanwise stations. The slipstream simulator was non-metric and was mounted to the floor of the wind tunnel by a strut which supported the simulator and housed the ejector drive air line. The drive air to the simulator was supplied from the NASA high pressure system. A heater was used to restore the total temperature lost during the throttling process to preclude the possibility of frost forming in the exit stream. The drive air was piped into the tunnel through a seven-inch diameter pipe which was used as a plenum chamber from which air was delivered up through the strut to the simulator. This seven-inch pipe was also used to support the strut and simulator. The strut was designed to fit around the pipe in a collar type arrangement that allowed longitudinal and lateral movement of the simulator strut. This movement permitted the simulator to be positioned at the desired location relative to the wing-body. An aerodynamic fairing was placed around the support pipe on the tunnel floor to minimize disturbances to the wing-body.

The slipstream simulator consisted of a nacelle enclosing an ejector comprised of 20 drive nozzle assemblies attached to the inner duct wall and spanning the outer 60% of duct radius. Removable sets of swirl vanes located downstream of the drive nozzles were used to produce angular velocity, or swirl, in the energized flow.

A remotely controlled translating rake containing total pressure probes and a flow direction probe was located downstream of the wing trailing edge The rake was computer controlled which positioned the rake and recorded the rake data. In addition to measuring the flowfield downstream of the wing,

the rake was used to measure and calibrate the exit flow from the isolated simulator as a function of drive pressure and swirl vane configuration.

4.1 Slipstream Simulator

The purpose of the simulator was to produce a flow simulating the slipstream of a highly loaded propeller typical of those currently under development by Hamilton Standard and NASA for use on aircraft cruising near Mach 0.8. A typical flowfield measured behind one of these propellers, operating at a disc loading, SHP/D_p^2, of $30/kw/m^2$ $\left(\frac{37.5\ HP}{ft^2}\right)$ is shown in Figure 3.[4] Peak total pressure ratios near 1.075 and swirl angles around 0.113 rad (6.5°) are present. For this test program a range of variables containing these values was chosen. Nominal swirl angles of 0.52, 0.105, and 0.157 rad (3°, 6°, and 9° , positive up inboard) and peak total pressure ratios of 1.000, 1.05, 1.075, and 1.100 were selected. A swirl (up outboard) of -0.105 rad (-6°) was also selected to investigate the effects of swirl direction.

To simulate this flowfield an ejector of the type shown on Figure 4 was selected. The propeller slipstream has the high energy air in the outer 60 percent of the slipstream cylinder. Therefore, the ejector drive nozzles were also located in the outer part of the internal duct to energize this part of the flow and leave an inner core of flow at freestream total pressure. Mixing between the two streams smoothed out the transition between the two energy streams. The swirl vanes downstream of the drive nozzles were used to produce the swirl in the stream.

4.1.1 Simulator Sizing - The exit nozzle diameter (or the simulated propeller diameter) was determined by scaling the model span by the ratio of the propeller diameter to wing span from the results of a recent systems study.[2] The D_p/b ratio from these studies was 0.117. The wind tunnel model span was 122 cm (48 in) resulting in a simulator exit diameter of 14.2 cm (5.6 in).

The maximum diameter of the simulator was kept as small as possible but large enough to avoid choking of the internal flow. It was necessary to minimize the external diameter because of the transonic test Mach numbers

and the need to minimize the interaction between the non-metric nacelle and the metric wing-body. Assuming an exit Mach number of one and an internal Mach number of 0.6, and allowing for the drive nozzle plenum chamber volume and material thickness, the resulting maximum diameter was 18.3 cm (7.2 in) and the internal diameter was 15.5 cm (6.12 in).

4.1.2 Simulator Design - The simulator was comprised of five separate sections as shown in Figure 4. These sections will be described starting at the aft end.

4.1.2.1 Exit Nozzle - Having selected the exit diameter and maximum internal and external diameter, it remained to select the nozzle length and shape. The length was found by using an external radial contraction ratio criteria of

$$\frac{R_{max} - R_{exit}}{length} = 0.1$$

and the external shape was determined by using a drafting spline set parallel to the simulator axis at the maximum radius (R_{max}) and terminating with an angle of 0.157 rad (9°) at the nozzle with (R_{exit}).

4.1.2.2 Swirl Vane Assembly - The swirl vanes and internal instrumentation were contained in this section. The swirl vanes were located in the maximum internal diameter section to avoid blockage and choking in the accelerating nozzle flow.

The swirl vanes were removable as an assembly which was retained by the nozzle section. The swirl vane assembly consisted of an outer and inner ring to which the vanes were attached.

The swirl vanes were designed using a two-dimensional cascade theoretical computer program.[5] The relationship between the swirl angle at the vane location and at the exit was found using the conservation of angular momentum. The angular momentum equation is

$$rV_t = rV \tan \phi = \text{constant}$$

As the flow travels from the swirl vanes to the exit it accelerates to a

higher velocity and shrinks to a smaller radius. Compressible flow relations were used to relate V to r. Using the above relationship the following results were obtained:

ϕ_{exit}	ϕ_{vanes}
0.052 rad (3°)	0.069 rad (4°)
0.105 (6)	0.141 (8.1)
0.157 (9)	0.213 (12.2)

For ϕ_{exit} = 0.105 rad (6°), the maximum section lift coefficient (c_ℓ) of the vanes was limited to 0.2 because of the low Reynolds number and small vane thickness to chord ratio ($\approx$ 3 percent). Using simple cascade theory[6]:

$$c_\ell = 2 \frac{S}{C} (\tan \phi_{vane})$$

this c_ℓ = .2 requirement could be satisfied if 20 vanes were used with a chord of 3.6 cm (1.4 in) at the outer radius (7.77 cm or 3.06 in). The vanes were tapered in proportion to the radius to maintain S/C constant as they spaned 60 percent of the internal duct radius measured from the outer wall.

The two-dimensional theoretical computer program[5] was used to set the amount of camber to produce the correct ϕ_{vane} values and yield identical pressures peaks on the suction and pressure surfaces at the leading edge. Vane realignments to the 0.105 rad (6°) set were made based on initial tests of the 0.157 rad (9°) set. The final designs are given in Table 1.

4.1.2.3 Mixing Section - The third section is an optional spacer interposed between the vanes and drive nozzles to provide length to achieve adequate mixing. The simulator could have been operated with any of three different lengths. The estimated mixing length of 20.3 cm (8 in) was determined experimentally to be adequate and the spacer providing this length was used throughout the test.

4.1.2.4 Drive Nozzle Assembly - The drive nozzles consisted of twenty struts brazed into a ring that forms the inner plenum wall. The struts extend across the outer 60 percent of the duct radius. The inner 40 percent was flow-through. Each strut was a brazed assembly of 21 tubes bent along a

gentle curve. The drive nozzles were formed by swaging the tube to the exit diameter. The exit diameter of the tubes varied along the radius.

The radial distribution of drive nozzle area was designed to produce the desired radial distribution of exit total pressure ratio. Figure 5 shows the design total pressure ratio distribution at $M_\infty = 0.8$. The radius between $\frac{r}{R} = 0.4$ & 1.0 was divided into three annular regions. The simulator exit Mach of each region was then selected to simulate the desired distribution. The drive nozzle area was chosen by using ejector parametric performance calculated by using a one-dimensional analysis computer program which included empirical loss factors. These results are summarized in Figure 6 in terms of simulator nozzle exit Mach number, M_5 (see Figure 4), versus drive pressure ratio, P_D/P_0, as a function of drive nozzle area ratio. A design drive pressure ratio of 8.8 was selected (which corresponds to drive pressure of 5.86×10^5 Pa or 85 psia), and the area ratios required to achieve the desired augmentation in the three annular regions were respectively 58, 50, 45. These area ratios, divided into the area of the annular duct regions, specified the primary jet exit areas for the regions. The calculations are summarized on Figure 5.

The number of drive nozzle struts is set by the need to achieve uniform circumferential mixing. Based on empirical criteria and previous ejector experience, it was determined that 20 struts would be adequate for complete mixing to occur within 20.3 cm (8 in).

4.1.2.5 Simulator Inlet - The inlet for the slipstream simulator was designed for efficient operation at the desired test conditions at Mach numbers of 0.7 to 0.84. The inlet design was constrained by the simulator diameter requirements as well as providing adequate airflow and drag divergence margins at all operating conditions. The internal throat area and lip thickness were sized to accommodate 5% more airflow than the estimated maximum airflow required by the internal ejector system. The external cowl was designed to have a drag divergence Mach number of 0.86 at an airflow condition that was 10% below the estimated minimum airflow flowing through the simulator with the power off. A maximum local Mach number of

0.86 for a freestream Mach number of 0.84 was determined from results of an off-body flowfield analysis using the Douglas Neumann Potential Flow Program[7] for a similar wing-body configuration. Critical dimensions of the inlet relative to the maximum radius 9.14 cm (3.6 in) are shown in Table II.

4.1.3 Simulator Instrumentation - The simulator instrumentation consisted of (1) external surface static pressures, used to determine whether severe adverse interference effects were experienced between the simulator and the fuselage of the wing body model, and (2) internal total and static pressures used to monitor operation of the simulator.

The ejector plenum was instrumented with two high pressure transducers and two copper constantan thermocouples. These were used to set ejector drive air pressure to achieve the desired exit conditions.

4.2 Support Strut

The support strut was designed to be thick enough to enclose the 2.54 cm (1 in) outside diameter (OD) high pressure drive air line used to power the ejector simulator. The thickness ratio and sweep of the strut were selected so that at a freestream Mach number of 0.84, the maximum surface Mach number would be subcritical. The airfoil shape normal to the leading edge of the strut was a NACA 0015 section (t/c = 15 percent) with a maximum thickness of 3.5 cm (1.375 in). The sweep was 0.7 rad (40°) resulting in a streamwise t/c of 11.50 percent. Anticipating unsweeping effects near the simulator, this streamwise t/c was reduced to eight percent at the intersection of the strut and the simulator. The eight percent was faired into the 11.5 percent in a distance equal to one simulator diameter.

4.3 Floor Mount and Floor Fairing

The support strut was attached to a 17.8 cm (7 in) OD tube which delivered drive air from the NASA high pressure air supply system to the 2.54 cm (1 in) OL pipe which goes up the strut to the simulator. The strut attachment to the 17.8 cm (7 in) pipe was a collar type arrangement to

permit lateral and longitudinal movement of the simulator. Sixty three cm (25 in) of fore and aft movement of the strut was available to allow the simulator to be located close to the wake rake for calibration and in front of the wing for testing. Lateral movement of 53.8 cm (21.2 in) from the vertical was also provided so that the simulator could be located on either side or the fuselage and to be positioned relative to the fuselage. The vertical orientation of the simulator exit relative to the wing was achieved by moving the wing-body with the tunnel sting support.

An aerodynamic fairing on the tunnel floor was designed to enclose this mounting system to minimize disturbances in the flowfield about the wing body. The shape of this fairing is illustrated with photographs of the tunnel installation. Figure 7 gives the calculated[8] velocity perturbations along the model centerline due to the floor fairing. No corrections for this small velocity increment are included in the data.

4.4 Wing Body Model

The wing body model (Figure 8) was a Douglas Aircraft model used previously in the Ames 11-Foot Wind Tunnel for supercritical wing development. Previous tests indicated good performance and very little drag creep up to the drag divergence Mach number. Figure 9 illustrates the drag characteristics obtained previously.

4.4.1 Wing Geometry - The wing planform is shown in Figure 8 with the pertinent wing parameters. The defining airfoil sections are given in Table III. Straight line interpolation is used between the defining sections. The airfoil sections are defined in the wing reference plane and the relationship of this plane to the fuselage is shown on Figure 10.

4.4.2 Wing Instrumentation - The wing was instrumented with 234 surface static pressures at six spanwise locations indicated on Figure 11. The pressure rows at 13, 35, and 65 percent semi-span were on the right side and the others were on the left side. This necessitated running the simulator on both sides of the fuselage to obtain a complete set of surface pressures in the presence of the slipstream.

4.5 Traversing Total Pressure Rake (Wake Rake)

A traversing rake was used to calibrate the slipstream simulator with the wing-body removed from the tunnel and to measure the flowfield downstream of the wing trailing edge with the slipstream simulator operating. A five hole flow angle probe was used during the simulator calibration to determine the swirl angle produced by various swirl vane sets.

The rake was comprised of 11 total and 10 static pressure orifices alternatively arranged and spaced at 1.27 cm (1/2 in) increments as illustrated in Figure 12. It was attached to the forward end of a separate sting which could be remotely pitched so that the tubes traversed an arc length of 3.05 cm (1.2 in). The sting in turn, was mounted to a carriage which could be moved laterally on two parallel remotely actuated lead screws. These screws were rigged with a sweep angle of 0.231 rad (13-1/4°) and a dihedral angle of 0.035 rad (2°) so that the rake followed the wing trailing edge during a lateral traverse. The traversing apparatus was attached to the model support sting downstream of the model. The pressure probes were connected to individual pressure transducers through three-position zero-operate-calibrate valves. The transducers and valves were mounted on the traversing carriage. The wake rake system was equipped with electric drive motors and position indicating potentiometers for remote operation. The position of the rake and acquisition of the pressure data was controlled by a Douglas owned SEL 810A computer system located in the wind tunnel control room.

The five-hole flow angle probe was mounted 7.12 cm (2.805 in) inboard of the basic wake rake. The probe is illustrated in Figure 13. It was parallel to, and in the plane of travel of, the center total head probe of the rake.

4.6 Swirl Vane Flow Test Rig

A swirl vane flow test rig was used to measure the swirl angles produced by the swirl vanes prior to installation in the simulator at Ames. This was to provide an opportunity to modify the swirl vane design prior to the wind tunnel test in the event undesirable flow conditions or instabilities were discovered.

4.6.1 Description of Test Rig - The test rig is illustrated on Figure 14. It consisted of a series of ducts attached to a centrifugal compressor. The air was delivered through the large pipe which turned the flow 1.57 rad (90°) and passed it through a honeycomb section which was installed to ensure uniform parallel flow at the exit. After passing through the honeycomb the ducting contracted to a diameter of 15.24 cm (6 in) where the swirl vanes were installed. The flow was then further contracted to the exit diameter of 14.2 cm (5.6 in). The flow exhausted vertically toward the ceiling which was about 13.7 m (45 ft) away from the nozzle exit.

The compressor had the capability of producing $M = 0.4$ at the swirl vanes. Anticipated tunnel test conditions at the vanes was $M = 0.6$.

4.6.2 Test Rig Instrumentation - The instrumentation used to measure the exit flow consisted of fluorescent mini-tufts with a diameter of 0.0018 cm (0.0007 in) attached to a thin wire stretched across the exit diameter and a laser Doppler velocimeter (LDV). The angle between the flow tufts installed at equal radii on opposite sides of the nozzle centerline were used as a first order check of flow angle. The LDV was later used for accurate measurements of the radial swirl distribution. The flow was observed to be very steady and repeatable, with no sign of instability.

4.7 NASA Ames 14-Foot Wind Tunnel

The Ames 14-foot wind tunnel is driven by a three-stage axial flow compressor powered by three electric motors mounted in tandem outside the tunnel. The air circuit is closed except for an air exchanger in the low speed section which is used to control the air temperature to approximately 46°C (115°F). The test section is 4.11 m (13.5 ft) high and 4.21 m (13.8 ft) wide. The tunnel was operated from 0.7 to 0.84 Mach number for this test. The airflow total pressure is always atmospheric resulting in a variable Reynolds number with Mach number. The Reynolds number versus Mach number recorded during this test is shown on Figure 15.

5.0 RESULTS AND DISCUSSION

5.1 Introduction to Test Results

The test apparatus described in Section 4.0 was installed in the Ames 14-foot tunnel. Various combinations of these parts were used during the test. The sequence of tests consisted of the following: initially the wing-body alone was tested to determine the proper boundary layer transition trip and to determine tunnel flow angularity. Next the wing-body was removed and the wake rake apparatus and simulator was installed. The flow angle probe was calibrated with the simulator positioned as far as possible from the probe (to the right about six nacelle diameters from the probe). The simulator was then repositioned in front of the rake and calibrated by surveying total pressure and swirl distributions across the exit. The wing-body was reinstalled and the wake rake data of the simulator-wing interaction was obtained. Finally the rake was removed and the force data on the wing-body was obtained in the presence of the simulator.

Because the simulator was non-metric, the baseline configuration for power incremental effects was assumed to be with the simulator installed at zero power and swirl. If increments from wing-body alone condition were used, then a non-metric interference force between the metric wing-body and non-metric simulator would be incorrectly included in the observed increments. Incorrect interferences due to power could also appear on the simulator for the power-off/power-on increments, however, this effect was indeterminable from the pressures measured on the nacelle. Another potential shortcoming of the simulation technique is the presence of the wake of the simulator flowing over the wing. However, since the wake did not vary with power, it was assumed that the incremental effects are valid. It must be remembered that the purpose of the test was to identify any large order-of-magnitude slipstream wing interaction effects and not to establish highly accurate results. The results to be shown later, however, are similar to those obtained in 1956[9] where an active propeller on a conventional wing was used.

5.2 Wing-Body Alone

The wing-body was installed in the tunnel without the rake or simulator present. However, the floor fairing was present. Forces and surface pressures were recorded through a series of pitch angles over the range of test Mach numbers from 0.70 to 0.84. The following data were derived from these tests.

5.2.1 Transition - A transition study was conducted to identify the minimum size roughness capable of effectively causing transition at the desired location. Boundary layer transition was fixed by strips of roughness elements composed of glass beads attached to the wing by brushing a suspension of the balls in colored lacquer. The strips were 0.32 cm (1/8 in) wide and located on the wing upper surface at 3.17 cm (1.25 in) from the leading edge or 15 percent of the local wing chord, whichever was least, and on the wing lower surface at 4.32 cm (1.7 in) from the leading edge. The trips were verified to be effective by Fluorene sublimation flow visualization. The minimum size roughness was determined to be beads with a diameter of 0.137 cm (.0054 in).

5.2.2 Flow Angularity - The model was run upright and inverted to determine flow angularity. A $\Delta\alpha$ correction of 0.003 rad (0.15°) was determined from C_L versus α plots and input into the data reduction program.

5.2.3 Force Data - The drag characteristics of the wing-body are shown on Figure 16 at C_L's of 0.4, 0.5, and 0.6. Drag characteristics are as expected for an advanced technology wing of this geometry. The drag rise Mach number, defined to be the Mach number at a drag slope $\Delta C_D/\Delta M$ of 0.1, is 0.8 and above. The wing also has excellent drag characteristics prior to drag rise with essentially no drag creep.

The lift curves at two Mach numbers are shown on Figure 17. The buffet onset (defined by the break in the lift curve) is at a C_L of 0.677 for $M_0 = 0.8$ illustrating excellent lifting capability for this wing.

5.2.4 Pressure Data - The wing surface pressures at the last linear point in the lift curve are plotted in Figure 18. The wing exhibits an extensive

supercritical flow region without the appearance of significant flow separations.

The span load at the same condition is shown on Figure 19.

5.3 Simulator Calibration

5.3.1 Static Swirl Vane Calibration - Because of the two-dimensional flow assumptions made during the vane design, these tests were used to check the actual flow angles obtained and based on these data, any remaining sets could be redesigned to insure that the desired angles were obtained. The first check occurred on the nominal 0.157 rad (9°) set and indicated peak swirl angles of 0.227 rad (13°). Based on this result, the 0.105 rad (6°) nominal set was modified to produce 0.127 rad (7°) peak swirl and the 0.052 rad (3°) set was not changed and was estimated to produce 0.07 rad (4°) and peak swirl Measured peak angles turned out to be 0.14 rad (8°) and 0.087 rad (5°), respectively.

5.3.2 Tunnel Installed Calibration - The flow angle probe was calibrated before the simulator was calibrated. With the simulator out of the presence of the rake, the flow angle probe was pitched using the tunnel sting and the differential static pressures on the probe conical surface, ΔC_p, recorded over a range of tunnel Mach numbers. A calibration of ΔC_p versus α was thereby obtained. During simulator calibration, the ΔC_p was recorded and the value of the swirl angle, α_s, determined.

During simulator calibration, the simulator was positioned so that the flow angle probe could be traversed across the simulator exit. The wing-body model was removed from the tunnel although the balance remained on the sting covered by a small fairing. The flow angle probe was located so that as the rake traversed horizontally, the probe would pass through the center of the exit nozzle. The streamwise location of simulator was set so that the probe would pass immediately behind the nozzle, which corresponded to the technique used by Hamilton Standard to make the measurements on the propeller. The simulator drive pressure, P_D, was set at selected values and the wake rake

traversed and the data recorded. The calibration data consisted of total pressure and swirl angle distributions. The internal simulator instrumentation (Figure 4) was not needed.

The total pressure data from rake probes located above and below the flow angle probe were examined for selected cases. These data gave total pressure distributions similar to tne flow angle probe but at several vertical positions relative to the simulator centerline. Analysis of these data confirmed that uniform circumferential mixing was being achieved.

Selected results of the simulator calibration are shown in Figures 20 through 22. Based on plots similar to these, a correlation of peak P_{T_J}/P_{T_O} (i.e., 1.095 on Figures 21 or 22) versus drive pressure (P_D/P_O) was made and used to find the P_D/P_O values for the selected P_{T_J}/P_{T_O} values of 1.000, 1.05, 1.075, and 1.10. The swirl angle used for reference was one-half the sum of the absolute values of the peak positive and negative values. There was small increase in the swirl angle with power so values selected were near the intermediate power setting of P_{T_J}/P_{T_O} = 1.05. There was an increment in swirl of approximately 0.007 rad (0.4°) for a P_{T_J}/P_{T_O} increment of 0.025. The measured swirl angles versus the nominal values are given below:

$\alpha_{S_{NOMINAL}}$	$\alpha_{S_{TUNNEL\ CALIBRATION}}$
.052 rad (3°)	.07 rad (4°)
.105 (6)	.122 (7)
-.105 (-6)	-.122 (-7)
.157 (9)	.192 (11)

The calibration results are compared to the nominal Hamilton Standard propeller operating conditions on Figure 23. The swirl angles are well represented but there is not enough total pressure in the outer part of the jet. This appears to be a consequence of the nacelle internal and external wake regions which are an undesirable but unavoidable consequence of the simulation technique.

The swirl angles are compared to the static data obtained using the LDV in Figure 24. The agreement is quite good except at the outer radius for the negative angle values. This difference is attributed to experimental inaccuracies in the static data.

To evaluate the rate at which the swirl angles and velocity profiles change with axial distance downstream of the simulator, the simulator was positioned further forward from the rake at distances corresponding to the wing quarter chord and wing trailing edge as measured along the centerline of the simulator. These results, shown on Figure 25, indicate very little change in the swirl and some smoothing of the total pressure profile due to mixing relative to the conditions present at the simulator exit.

5.4 Simulator-Wing-Body Combination

5.4.1 Tunnel Installation and Test Procedure - The wake survey data were obtained with the rake-wing-body and simulator installed. No force data were taken during these runs. Wake rake data was taken at 0 and .122 rad (7°) swirl only and at limited Mach numbers because of the time required to obtain this data. To obtain the force data, the rake was removed and a complete series of angle of attack and simulator exit conditions were run. Because half the wing surface pressures were located on each wing (Figure 11), the simulator had to be placed on both sides of the fuselage to obtain a complete set of surface pressure data. The opposite side runs were limited to the 0 and .122 rad (7°) swirl cases.

Drive pressures were set which corresponded to the appropriate values of the exit conditions obtained from the previous calibration runs.

5.4.2 Test Results

5.4.2.1 Force Data - The force results are presented as increments from the simulator installed condition at zero power which corresponded to a jet pressure ratio $P_{T_J}/P_{T_0} = 1.0$ and swirl angle, $\alpha_s = 0$. The increase in the skin friction drag (scrubbing drag) due to the difference in the slipstream dynamic pressure and the freestream was estimated and removed from the power-on experimental increments. The increments obtained with the

simulator on one side have been doubled to represent a two engine configuration. Doubling the drag is an approximation since the drag of a two engine configuration is not exactly twice the value of a slipstream on one side. However, it is a close approximation consistent with the exploratory nature of the test. This subject will be discussed again in Section 5.4.3.

The wing body drag characteristics with the simulator at zero power are shown on Figure 26. The drag rise Mach numbers based on a $\Delta C_D/\Delta M$ of 0.1 are slightly higher than for the wing body alone case because of the presence of the non-metric simulator.

The incremental drag results at three lift coefficients for various pressure ratios and swirl angles are shown on Figures 27 through 29.

There is very little dependence of the drag increment on C_L or M_o, even above the drag divergence Mach number of the wing body. Therefore, the drag rise characteristics of the wing-body are unaffected by the presence of the slipstream. Also, the increments are generally within 20 counts (0.0020) or about six percent of the wing body drag. Because of the nature of a supercritical wing operating at transonic Mach numbers and near drag divergence it was expected prior to the test that a substantially greater drag penalty might have occurred and that the penalties would be a strong function of the freestream Mach number.

Since the data are weak function of M_o and C_L, the data will be summarized at selected values of these variables. Specifically the conditions selected are $M_o = 0.8$ and an average value of the three C_L's.

The effects of pressure ratio and swirl are summarized on Figures 30 and 31. Figure 30 indicated that high swirl angles, around 0.196 rad (11°) actually produce a favorable drag increment (less drag with power than without). This result was confirmed by analytical calculation as will be discussed later in Section 5.4.3. This can occur because the local lift vector must always be perpendicular to the local onset flow. Where there is large upwash due to swirl the wing carries additional lift and it is rotated

in a forward direction relative to the flight path. This forward vector direction can produce thrust. On the downwash side the magnitude of the lift is diminished since the local section is operating at a reduced angle of attack and the rearward rotation of the lift vector has a small compensating effect. Large swirl angles do mean less axial thrust from the propeller, so a careful trade must be made.

The results at lower swirl angles show a drag increase. A swirl angle of 0.122 rad (7°) at a P_{T_J}/P_{T_0} = 1.075 has about .0010 more drag than the wing body. Other adverse effects have apparently overcome any favorable effects due to lift vector rotation at these lower swirl angles. The effect of a pressure ratio of 1.075 at zero swirl is to increase the drag by 0.0003. Therefore, the effect of 0.122 rad (7°) of swirl is to increase the drag by 0.0007.

The opposite direction swirl, up-outboard, data is also shown on Figure 30. The drag increments are larger indicating that the up-inboard swirl may be the preferred swirl direction.

Figure 31 is a cross-plot of the previous figure as a function of pressure ratio. This figure indicates that there is not a significant effect of pressure ratio.

The incremental lift results are very small as shown on Figure 32. Again there is little effect due to pressure ratio or Mach number. Swirl angles around 0.07 rad (4°) seem to produce the minimum lift increment.

5.4.2.2 Pressure Data - The pressure distributions are shown at four of the six spanwise locations. The data at 13% and 85% semispan were not affected by the simulator variables. The simulator slipstream extends from 31% to 55% of the semispan which places the stations at 35.5% and 50% within the slipstream. Only selected cases can be shown since half the wing pressure rows were on each wing so only limited full span data was obtained by placing the simulator on the opposite side of the fuselage.

The effects due to power at M_0 = 0.7 and 0.8 are shown on Figures 33 and 34 for a fixed angle of attack. At Mach 0.8 the shock on the wing is affected which contributes to the small .0003 drag increase obtained at this condition. The effect of the simulator without power on the wing has been to move the shock forward in the region downstream of the simulator as can be seen by comparing the isolated wing pressures shown on Figure 18 (which are at a slightly higher angle of attack) with those shown in Figure 34 at a P_{T_J}/P_{T_0} = 1.000.

The effects due to swirl are shown on Figures 35 and 36. Much more significant effects can be seen here. The inboard location within the jet (35.5%) indicates large effects due to swirl while the outboard location at 50% does not. No large separations are indicated based on these surface pressure data. Data at a lower angle of attack, shown on Figure 37, indicates similar trends to that obtained at higher angles.

Figures 38 and 39 focus on the effects of swirl at constant P_{T_J}/P_{T_0}. Figure 38 illustrates the effects of 0.122 rad (7°) swirl and Figure 39 illustrates the effect of 0.192 rad (11°) swirl relative to 0.122 rad (7°) swirl. The increment from 0.122 rad (7°) to 0.192 rad (11°) is small and yet the drag variation was significant. The data at 35.5% was not obtained for the 0.192 rad (11°) case which may have helped understand these effects.

The span loads at M = 0.7 and 0.8 and a fixed angle of attack are shown on Figures 40 and 41. The trends are predictable for each condition For example, the loading with power is increased relative to the no power case over the region of the slipstream. Also at the 35.5% semispan station, up inboard swirl increases the loading and up outboard (down inboard) decreases the loading. Some detail of the rapid variations that might be occurring is lost due to having only six spanwise pressure rows.

5.4.2.3 Wake Rake Data - The data obtained using the wake rake is shown on Figures 42 and 43 for P_{T_J}/P_{T_0} = 1.075 with zero and 0.122 rad (7°) of swirl. The lines are isobars of the ratio P_T/P_{T_0}. Key features of the data are the low energy regions of the wing and simulator/support system. The low

energy region outside the slipstream for the simulator would not be present for an active propeller. However, the active propeller would have a low energy region inside the slipstream due to the nacelle body. Since static pressure disturbances are transmitted through the outer simulator wake, disturbances in the slipstream can be transmitted to the rest of the wing. Also, as will be discussed in Section 5.4.3, using analytical methods, the effects of these wakes were estimated to be small.

The high energy regions due to the simulated propeller slipstream are shown by the P_T/P_{T_0} boundary of 1.0 and greater. In Figure 42 where there is no swirl, the jet shape is still annular as it was when it left the simulator but has been displaced by the spanwise flow induced by the finite wing shed vorticity. The size and shape of the slipstream was essentially unchanged at lower Mach numbers and angles of attack. In addition, more detailed analysis of the slipstream region revealed that peak P_T/P_{T_0} values were unchanged with M_0 and α_{FRP} variations and within .005 of the isolated values. These results indicate that there were negligible losses within the slipstream for these conditions.

For the case with swirl shown on Figure 43, the shape and size of the region greater than 1.00 is significantly distorted and reduced in size. Comparing the swirl and no-swirl cases and plotting only the P_T/P_{T_0} boundaries of 1.0 and greater as shown on Figure 44, illustrates that the 1.04 boundary is significantly smaller implying losses within the slipstream. A large low energy region of $P_T/P_{T_0} < 1.0$ is observed above the wing on the inboard side of the slipstream suggesting that there is a flow separation. This separation and attendant losses have contributed to the seven count (.0007) increase in the drag attributed to swirl as discussed previously.

Unlike the zero swirl case, reductions in M_0 and α_{FRP} reduced the size of the low energy region and increased the size of the high energy slipstream region as shown on Figures 45 and 46.

Unfortunately, efficient use of tunnel occupancy time necessitated obtaining the wake rake data prior to obtaining the force data. Therefore,

the rake data was only obtained for the nominal propeller swirl angle of 0.122 rad (7°) and the favorable effect due to the 0.192 rad (11°) swirl condition was not observed until the force data was obtained and the wake rake had been removed.

5.4.2.4 Oil Flow Visualization - Fluorescent oil flow visualization runs were made on the right hand wing upper surface with the simulator installed. The fluorescent oil was dispensed during the run from a sintered metal strip installed flush in the wing leading edge. Because of the tendency of the oil to foul the pressure orifices, this was done only at the conclusion of the test using the simulator configuration installed at that time.

Comparisons of the power-on and power-off conditions without swirl at $M_0 = 0.8$, $\alpha_{FRP} = 0.052$ rad (3°) shown on Figure 47 indicate little or no effect in the visual data of the jet scrubbed portion of the wing. Well up the drag rise, at $M_0 = 0.84$, an increase in the trailing edge separation is evident as illustrated on Figure 48. However, by inference from the force data, this separation is no worse than that which would be experienced by the isolated wing.

5.4.3 Comparison of Theory and Data - The test data has been compared to a theoretical solution developed in-house by Douglas Aircraft. The theory is restricted to wings alone and incompressible flow. This theoretical model is based on lifting line theory and has the capability of accounting for an arbitrary onset flow. The onset velocities are only specified in the plane of the wing. The uniform freestream flow was input over the regions outside the slipstream area and the propeller (or simulator) flow is input in the region of the slipstream. For the current test, the program was used to compare incremental lift and drag effects and to estimate the effects of the wake and the assumption of doubling the "one-side-only" result. Span loads are also compared but it must be remembered that the theory does not account for the simulator nacelle body effects. Therefore, increments are a more meaningful output of the program.

5.4.3.1 Force Data - The incremental force results are shown on Figures 49 and 50. Figure 49 indicates that there is little effect of power without

swirl while positive swirl (up-inboard) results in a drag reduction and negative swirl (up-inboard) results on a drag increase. Experimentally, other interferences prevent these trends from being followed but a swirl angle of 0.192 rad (11°) does produce a negative drag increment.

The increments in the lift, shown on Figure 50, are small. The experimental minimum lift at 0.07 rad (4°) swirl is not confirmed analytically.

Theoretically, the effect of removing the simulator nacelle wake ($P_{T_J}/P_{T_0} < 1$ on Figure 21) and the validity of doubling the drag increment on one side are given on Table IV. Based on this theoretical analysis, it may be concluded that the wake has a negligible effect on the results and that doubling the result obtained on one side is an adequate approximation.

5.4.3.2 Span Loading - The span loading of the clean wing (no nacelle) compared very well with the test data as shown on Figure 51.

The theoretical effect of power only with no swirl is shown on Figure 52. The negative increments are due to the nacelle wake and the positive increments are due to increased slipstream velocities. The test data had insufficient spanwise pressure rows to obtain the detail obtained analytically. However, referring back to Figure 40, the predicted increments in load seem to be somewhat higher than obtained experimentally.

The effects of swirl are shown on Figure 53. The test data have also been indicated on this figure. The level of the theory is different due to its inability to model nacelle body effects but the trends are correct if somewhat overpredicted again.

The effect of the nacelle wake on the span load is negligible everywhere except in the immediate vicinity of the wake as indicated on Figure 54.

6.0 CONCLUSIONS AND RECOMMENDATIONS

It is concluded that an ejector-nacelle propeller simulator similar to the one presented in this study can be successfully designed to produce a slipstream flowfield representing an active propeller. The following conclusions can be drawn from the force data:

- Incremental drag (ΔC_D*) due to power for a two-engine configuration at the nominal propeller conditions (P_{T_J}/P_{T_O} = 1.075, α_s = 0.122 rad (7°)) was about .0010 or 3% of the wing-body drag.
- There was no significant effect of C_L or M_O on the incremental force results.
- The effects on the force and pressure data due to swirl were more significant than due to pressure ratio.
- Swirl angles of 0.192 rad (11°) produced a reduction in drag.
- Swirl angles of 0.122 rad (7°) produced 7 counts (.0007) more drag than the same power condition with zero swirl.
- Up-inboard swirl generally had less drag than up-outboard swirl.
- Incremental lift effects were small; on the order of ΔC_L* = 0.025.
- Analysis indicates that the effect of the nacelle wake was negligible and it was sufficiently accurate to double the "one-side only" result.

The following conclusions can be made regarding the wing pressure distributions and wake rake data:

- The presence of the simulator without power affected the wing surface pressures producing less critical flow conditions downstream of the simulator than if the wing were in freestream flow.
- Wing surface pressure variations due to power were essentially restricted to the region within the slipstream.
- Wing surface pressure variations due to swirl were much larger at the inboard location than at the outboard location.

- Experimental span load variations were as expected but somewhat less than predicted analytically.
- The wake rake data indicated small effects due to power but revealed that up-inboard swirl produced a low energy region above the wing on the inboard side of the slipstream possibly indicating a flow separation.

Three recommendations are made:

- A test with an active propeller needs to be conducted to verify the validity of the test technique used here. During this test, careful attention must be given to the thrust-drag accounting system used and the technique used to calibrate the propeller.
- Using applicable theoretical tools, develop revised wing contours that will potentially reduce the separated region occurring when swirl is present and conduct another experimental program employing these revised wing contours in the presence of an engine nacelle body attached to the wing.
- Derive scaling laws to be applied to the data to estimate characteristics of other configurations.

7.0 REFERENCES

1. Kraus, E.F. and Van Abkoude, J.C.: Cost/Benefit Tradeoffs for Reducing the Energy Consumption of the Commercial Air Transportation System. Douglas Aircraft Company. NASA CR-137925. June, 1976.

2. Energy Consumption Characteristics of Transports using the Prop-Fan Concept. The Boeing Commercial Airplane Company. NASA CR-137938. November, 1976.

3. Hopkins, J.P. and Wharton, H.E.: Study of the Cost/Benefit Tradeoffs for Reducing the Energy Consumption of the Commercial Air Transportation System. Lockheed California Company. NASA CR-137927. August, 1976.

4. Rohrback, Carl: A Report on the Aerodynamic Design and Wind Tunnel Test of a Prop-Fan Model. AIAA Paper 76-667. July, 1976.

5. Giesing, J.P.: Extension of the Douglas Neumann Program to Problems of Lifting, Infinite Cascades. Douglas Aircraft Report LB 31653. July, 1964.

6. Robinson, A. and Laurmann, J.A.: Wing Theory. Cambridge University Press. 1956. p. 147.

7. Hess, J.L.: Calculation of Potential Flow about Arbitrary Three-Dimensional Lifting Bodies. Prepared under Contract N00019-71-C-0524 for Naval Air Systems Command. McDonnell Douglas Report MDC J5679-01. October, 1972.

8. Hess, J.L. and Martin, R.P.: Improved Solution for Potential Flow about Arbitrary Axisymmetric Bodies by the Use of Higher-Order Surface Source Method. Douglas Aircraft Company. NASA CR-134694. July, 1974.

9. Edwards, G.G., et al: The Results of Wind Tunnel Tests to a Mach Number of 0.9 of a Four Engine Propeller Driven Airplane Configuration Having 40° of Sweep-Back on an Aspect Ratio of 10. NASA TN 3789. 1956.

TABLE I

SWIRL VANE GEOMETRY

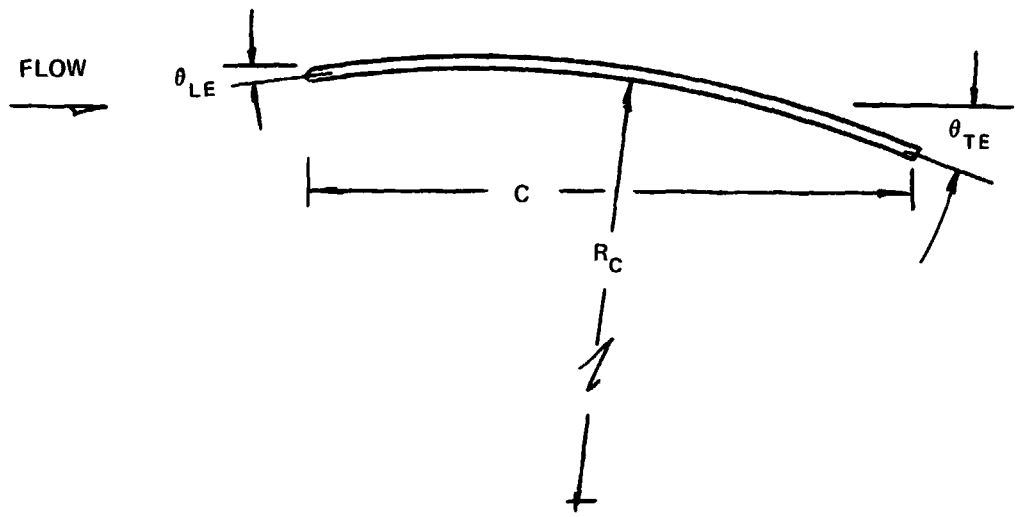

NOMINAL SWIRL VANE SET	$R_{C_{OUTER}}$ ①	$R_{C_{INNER}}$ ①	C_{OUT}	C_{IN}	θ_{LE}	θ_{TE}
0.052 RAD (3 DEG)	27.18 CM (10.703 IN.)	10.87 CM (4.281 IN.)	3.56 CM (1.40 IN.)	1.42 CM (0.56 IN.)	0.026 RAD (1.5 DEG	0.105 RAD (6 DEG)
0.105 [2] (6 DEG)	14.59 (5.744)	5.84 (2.298)	3.56 CM (1.40 IN.)	1.42 CM (0.56 IN.)	0.075 (4.3 DEG)	0.169 (9.7 DEG)
0.157 (9 DEG)	10.24 (4.031)	4.09 (1.612)	3.56 CM (1.40 IN.)	1.42 CM (0.56 IN.)	0.061 (3.5 DEG)	0.288 (16.5 DEG)

[1] R_C VARIED LINEARILY WITH LENGTH

2 MINUS 0.105 RAD SET TURNED IN OPPOSITE DIRECTION

TABLE II
INLET GEOMETRY

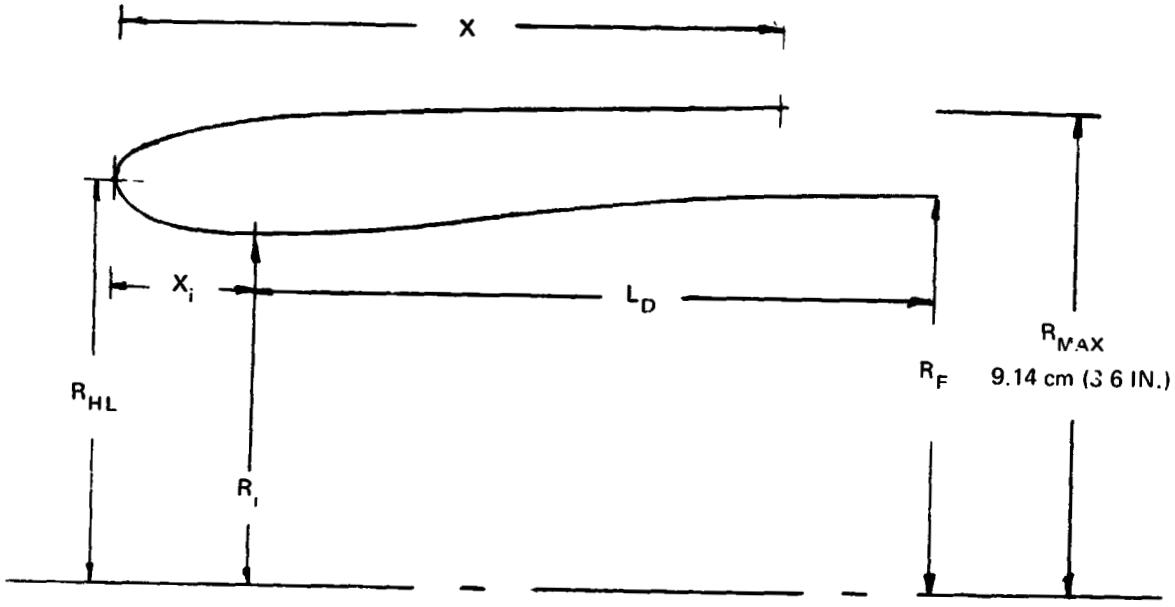

R_{HL}/R_{MAX} = 0.85

R_i/R_{MAX} = 0.81

L_D/R_{MAX} = 1.02

X_i/R_{MAX} = 0.08

R_F/R_{MAX} = 0.85

X/R_{MAX} = 1.01

TABLE III
AIRFOIL COORDINATES

	% CHORD	0.12b/2		0.35 b/2		0.70 b/2		1.00 b/2	
		X	Y	X	Y	X	Y	X	Y
UPPER SURFACE	100	13.66	−1.6796	13.86	−0.5679	17.17	−0.3164	20.01	−0.1157
	97.5	13.37	−1.6223	13.66	−0.5068	17.04	−0.2798	19.93	−0.0975
	95	13.08	−1.5527	13.46	−0.4501	16.91	−0.2442	19.86	−0.0806
	92.5	12.79	−1.4795	13.26	−0.3995	16.77	−0.2123	14.78	−0.0647
	90	12.50	−1.4058	13.06	−0.3538	16.64	−0.1838	19.70	−0.0505
	85	11.91	−1.2602	12.67	−0.2735	16.37	−0.1344	19.54	−0.0267
	80	11.33	−1.1187	12.27	−0.2045	16.10	−0.0927	19.38	−0.0074
	75	10.75	−0.9833	11.87	−0.1456	15.83	−0.0579	19.22	0.0079
	70	10.17	−0.8554	11.47	−0.0960	15.56	−0.0293	19.06	0.0196
	65	9.59	−0.7354	11.07	−0.0550	15.29	−0.0066	18.91	0.0280
	58.5	8.83	−0.5915	10.56	−0.0162	14.94	0.0141	18.70	0.0341
	55	8.42	−0.5186	10.28	0.0006	14.75	0.0224	18.59	0.0358
	50	7.84	−0.4218	9.78	0.0174	14.48	0.0296	18.43	0.0357
	45	7.26	−0.3323	9.48	0.0275	14.22	0.0325	18.27	0.0334
	40	6.68	−0.2501	9.08	0.0313	13.95	0.0313	18.12	0.0288
	35	6.10	−0.1747	8.68	0.0282	13.68	0.0258	17.96	0.0220
	30	5.51	−0.1061	8.29	0.0187	13.41	0.0156	17.80	0.0125
	25	4.93	−0.0451	7.89	0.0001	13.14	0.0001	17.64	0.0000
	20	4.35	0.0066	7.49	−0.0263	12.87	−0.0213	17.48	−0.0156
	15	3.77	0.0364	7.09	−0.0631	12.60	−0.0491	17.32	−0.0349
	10	3.19	0.0105	6.69	−0.1148	12.33	−0.0867	17.17	−0.0594
	7.5	2.89	−0.0335	6.49	−0.1501	12.20	−0.1127	17.09	−0.0753
	5.0	2.60	−0.1058	6.30	−0.1949	12.06	−0.1429	17.01	−0.0942
	2.5	2.31	−0.2308	6.10	−0.2601	11.93	−0.1873	16.93	−0.1204
	1.25	2.17	−0.3422	6.00	−0.3126	11.86	−0.2226	16.89	−0.1406
	.50	2.08	−0.4548	5.94	−0.3625	11.82	−0.2555	16.87	−0.1593
	.25	2.05	−0.5145	5.92	−0.3905	11.81	−0.2739	16.86	−0.1697
	.05	2.03	−0.5896	5.90	−0.4298	11.80	−0.2998	16.85	−0.1841
	0	2.02	−0.6507	5.90	−0.4523	11.79	−0.3208	16.85	−0.1956
LOWER SURFACE	.05	2.03	−0.7124	5.90	−0.4924	11.80	−0.3416	16.85	−0.2069
	.25	2.05	−0.7949	5.92	−0.5334	11.81	−0.3683	16.86	−0 2215
	.50	2.08	−0.8558	5.94	−0.5639	11.82	−0.3882	16.87	−0.2324
	1.25	2.17	−0.9853	6.00	−0.6212	11.86	−0.4252	16.89	−0.2526
	2.5	2.31	−1.1405	6.10	−0.6849	11.93	−0.4664	16.93	−0.2745
	5.0	2.60	−1.3540	6.30	−0.7662	12.06	−0.5183	17.01	−0.3017
	7.5	2.89	−1.4929	6.49	−0.8200	12.20	−0.5519	17.09	−0.3185
	10	3.19	−1.5906	6.69	−0.8603	12.33	−0.5767	17.17	−0.3306
	15	3.77	−1.7161	7.09	−0.9159	12.60	−0.6098	17.32	−0.3452
	20	4.35	−1.7938	7.49	−0.9526	12.87	−0.6302	17.48	−0.3528
	25	4.93	−1.8406	7.89	−0.9777	13.14	−0.6434	17.64	−0.3563
	30	5.51	−1.8646	8.29	−0.9948	13.41	−0.6506	17.80	−0.3564
	35	6.10	−1.8730	8.68	−1.0028	13.68	−0.6524	17.96	−0.3536
	40	6.68	−1.8703	9.08	−1.0032	13.95	−0.6488	18.12	−0.3478
	45	7.26	−1.8600	9.48	−0.9935	14.22	−0.6387	18.27	−0.3386
	50	7.84	−1.8438	9.88	−0.9735	14.48	−0.6218	18.43	−0.3251
	55	8.42	−1.8230	10.28	−0.9383	14.75	−0.5949	18.59	−0.3065
	58.5	8.83	−1.8067	10.56	−0.9058	14.94	−0.5708	18.70	−0.2897
	65	9 59	−1.7748	11.07	−0.8283	15.29	−0.5146	18.91	−0.2536
	70	10.17	−1.7501	11.47	−0.7581	15.56	−0.4644	19.06	−0.2213
	75	10.75	−1.7255	11.87	−0.6841	15.83	−0.4116	19.22	−0.1877
	80	11.33	−1.7023	12.27	−0.6135	16.10	−0.3612	19.38	−0.1557
	85	11 91	−1.6825	12.67	−0.5537	16.37	−0.3181	19.54	−0.1280
	90	12.50	−1.6695	13.06	−0.5145	16.64	−0.2889	19.70	−0.1082
	92.5	12.79	−1.6670	13.26	−0.5095	16.77	−0.2842	19.78	−0.1043
	95	13.08	−1.6683	13.46	−0 5179	16.91	−0.2884	19.86	−0.1064
	97.5	13.37	−1.6750	13.66	−0.5425	17.05	−0.3039	19.93	−0.1155
	100	13.66	−1.3957	13.06	0.5839	17.17	−0.3324	20.01	−0.1316

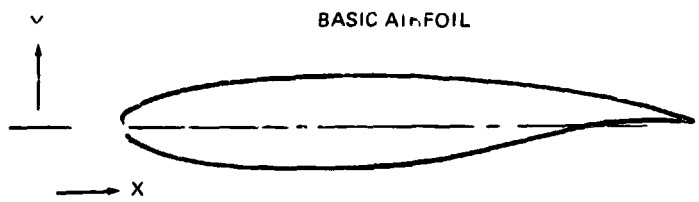

TABLE IV

THEORETICAL EFFECTS OF THE NACELLE WAKE AND DOUBLING "ONE-SIDE-ONLY" VALUE

M_o = INCOMPRESSIBLE

$@C_L$ = 0.5

P_{T_J}/P_{T_O} = 1.075

α_{SWIRL} = 0.122 RAD (7 DEG)

CASE	NACELLE WAKE	$\Delta C_{D_{THEORY}}$	$\Delta C_{L_{THEORY}}$
ONE SIDE DOUBLED	YES	-18×10^{-4}	0.016
ONE SIDE DOUBLED	NO	-18×10^{-4}	0.022
SOLUTION FOR BOTH SIDES	YES	-17.5×10^{-4}	0.016

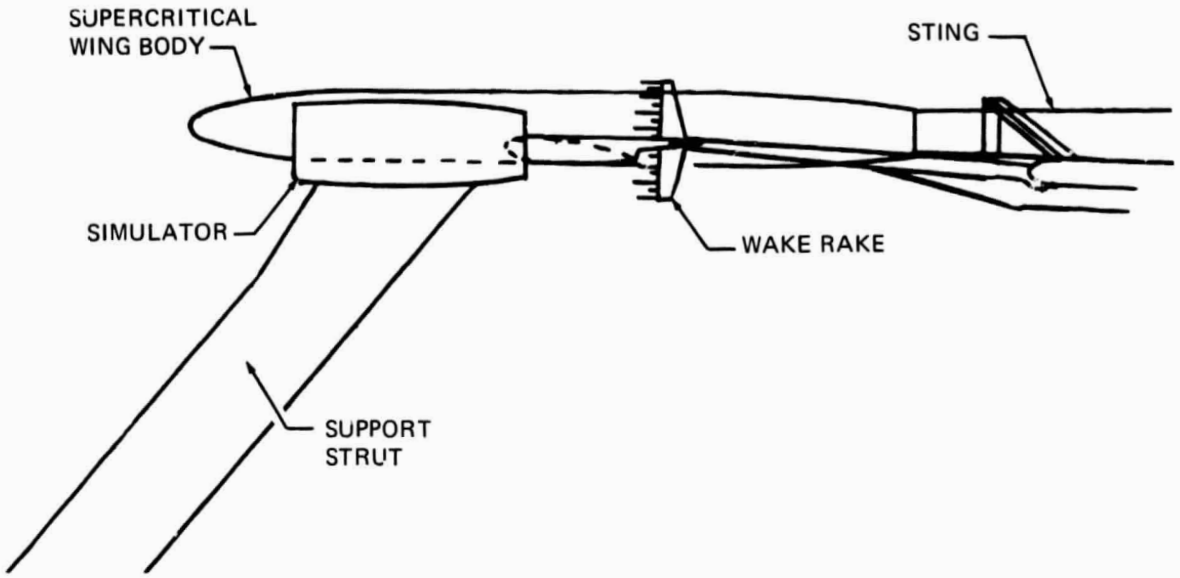

FIGURE 1. SKETCH OF WIND TUNNEL MODEL

FIGURE 2. PHOTOGRAPH OF MODEL INSTALLATION FROM UPSTREAM OF THE MODEL

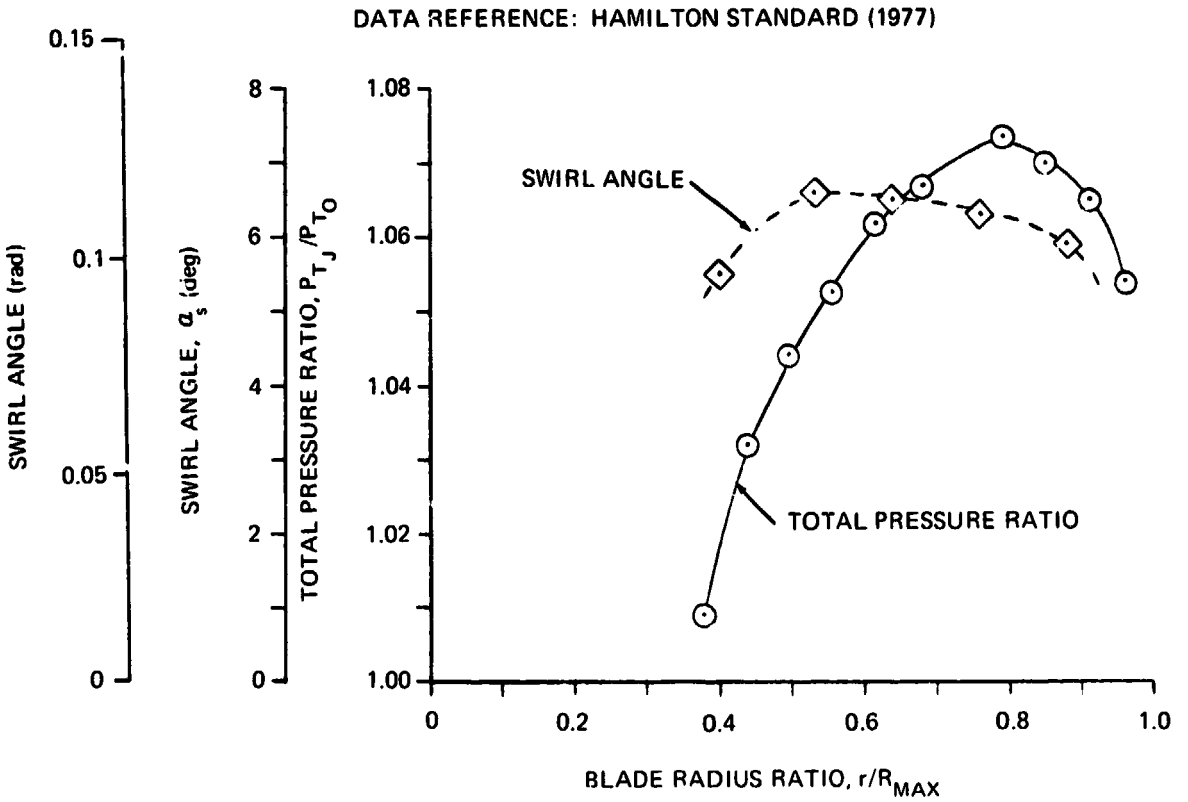

FIGURE 3. ACTIVE PROPELLER FLOW FIELD

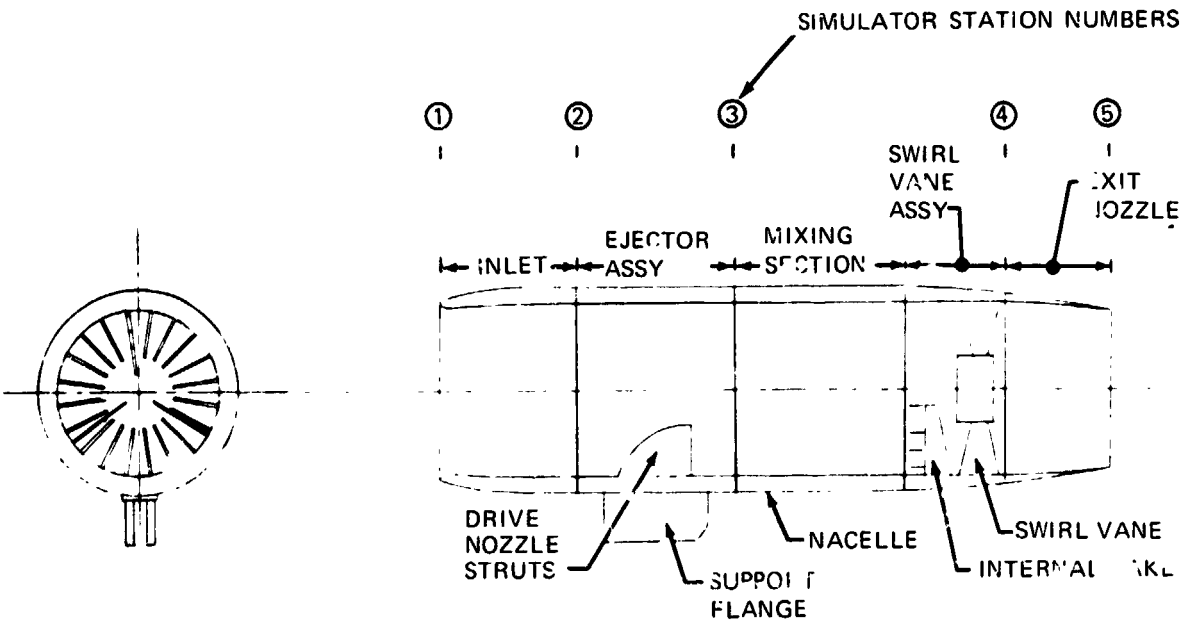

FIGURE 4. DESCRIPTION OF EJECTOR SIMULATOR

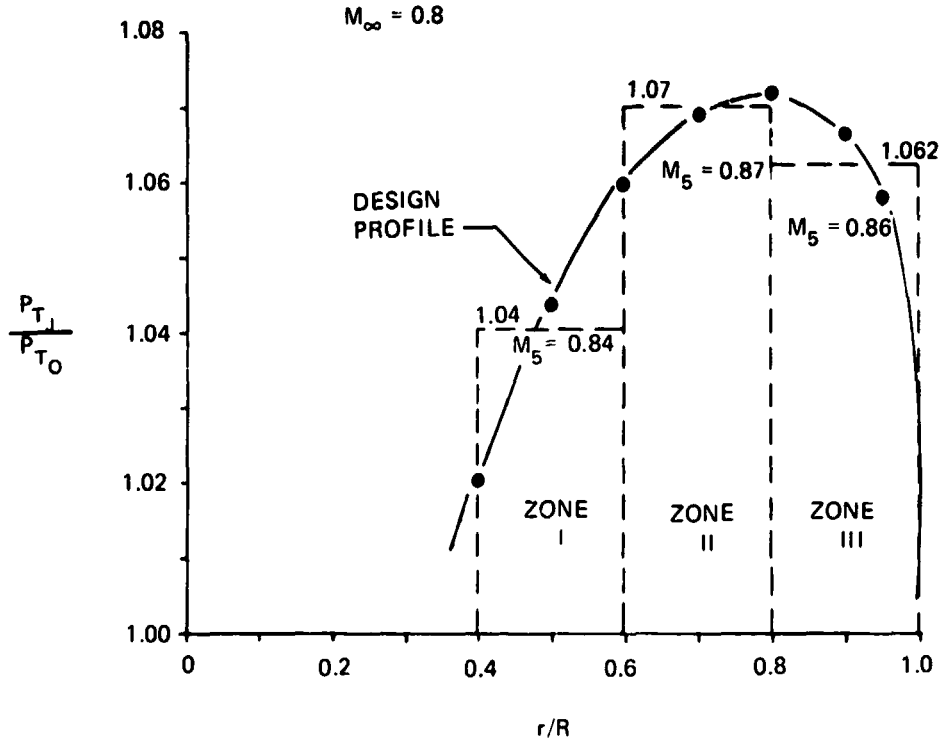

$P_D/P_O = 8.8$

ZONE	M_5	A_3/A_D
I	0.84	58
II	0.87	50
III	0.86	45

$A_{3_I} = 37.96\ cm^2$ (5.883 IN.^{2})

$A_{3_{II}} = 53.14$ (8.237)

$A_{3_{II}} = 68.33$ (10.590)

$A_{D_I} = 0.654/20 = 0.0327\ cm^2$ / PER STRUT (0.0050 IN.^{2})

$A_{D_{II}} = 1.328/20 = 0.0664$ (.0103)

$A_{D_{III}} = 1.518/20 = 0.0759$ (.0118)

FIGURE 5. DRIVE NOZZLE DESIGN PARAMETERS

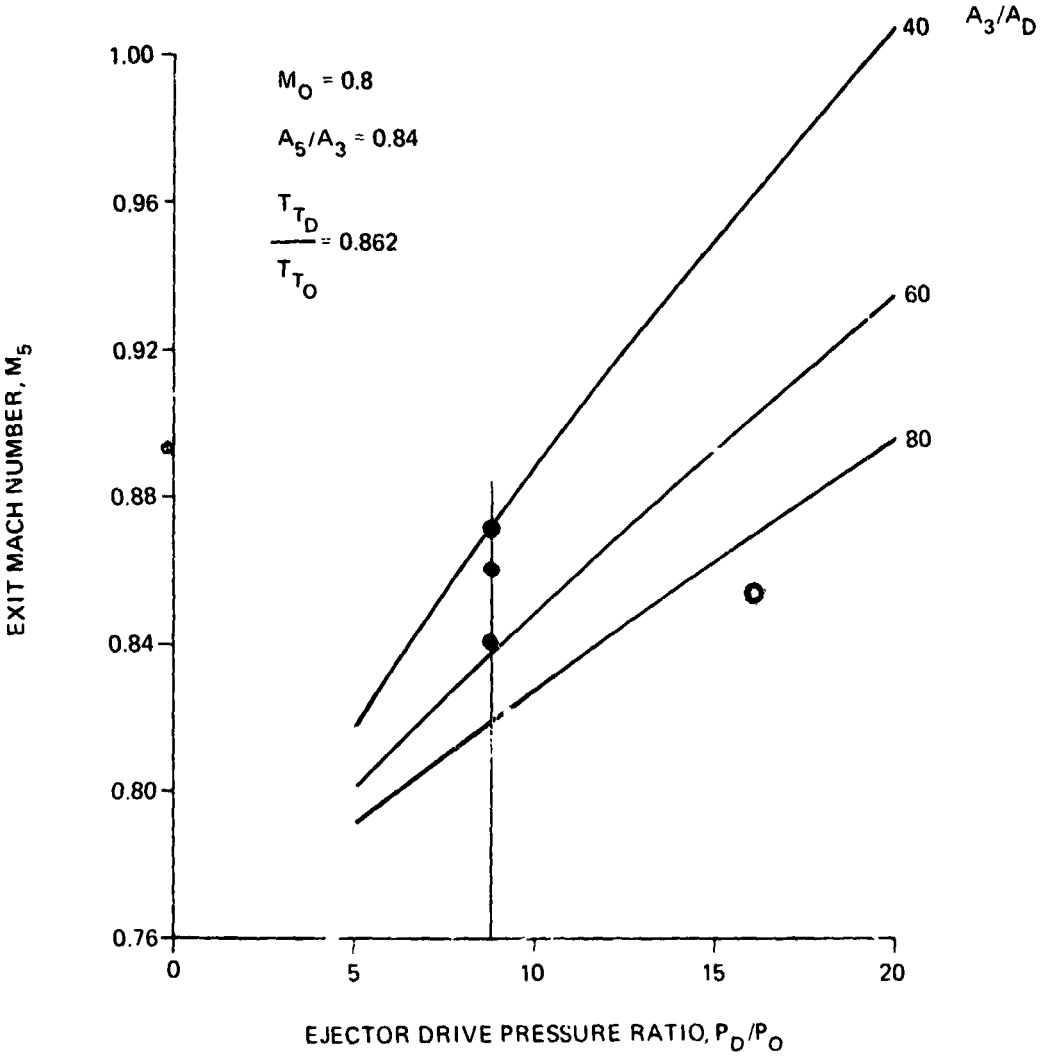

FIGURE 6. THEORETICAL ONE DIMENSIONAL EJECTOR PERFORMANCE

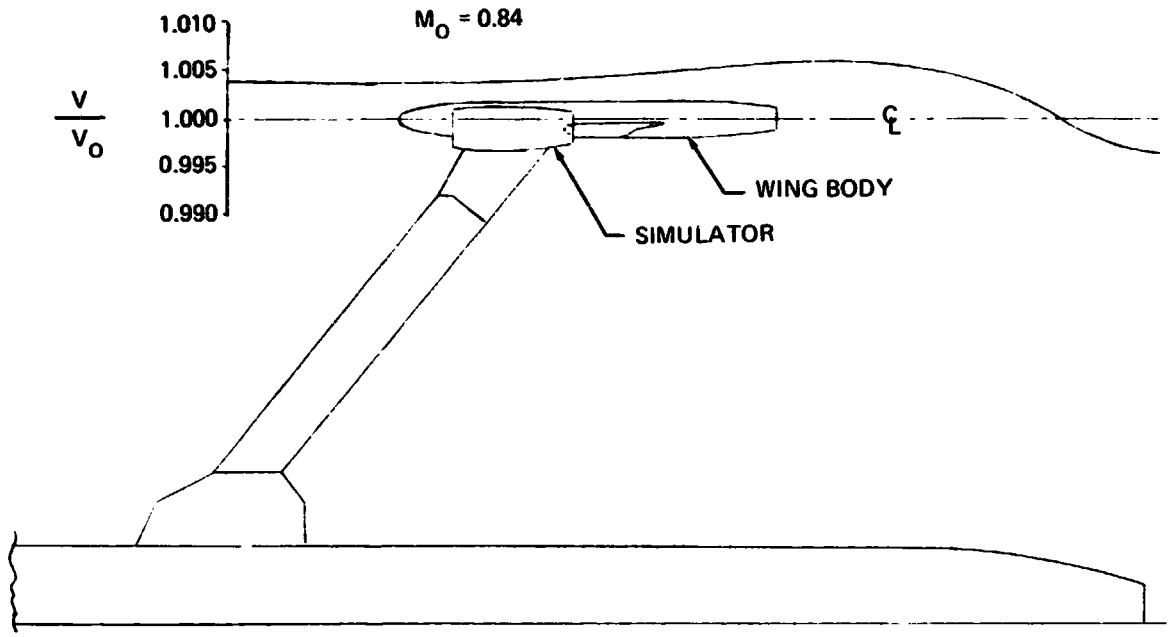

FIGURE 7. VELOCITY INCREMENT AT MODEL CENTERLINE DUE TO FLOOR FAIRING

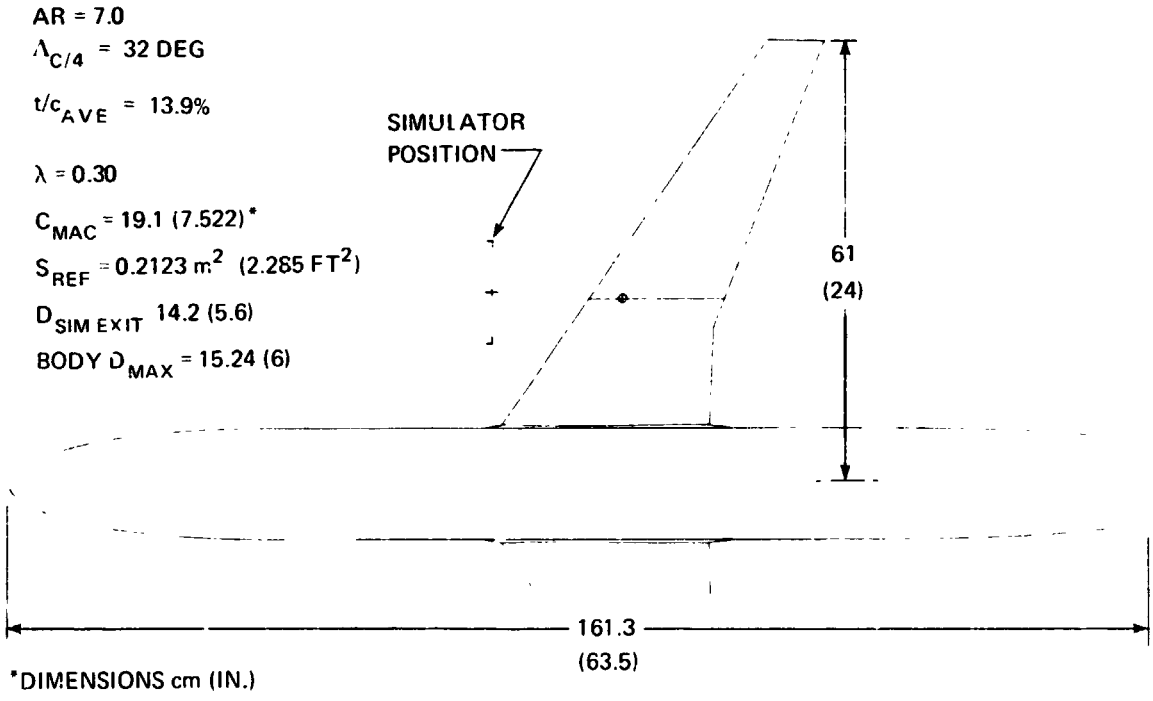

FIGURE 8. ILLUSTRATION OF WING-BODY PLANFORM

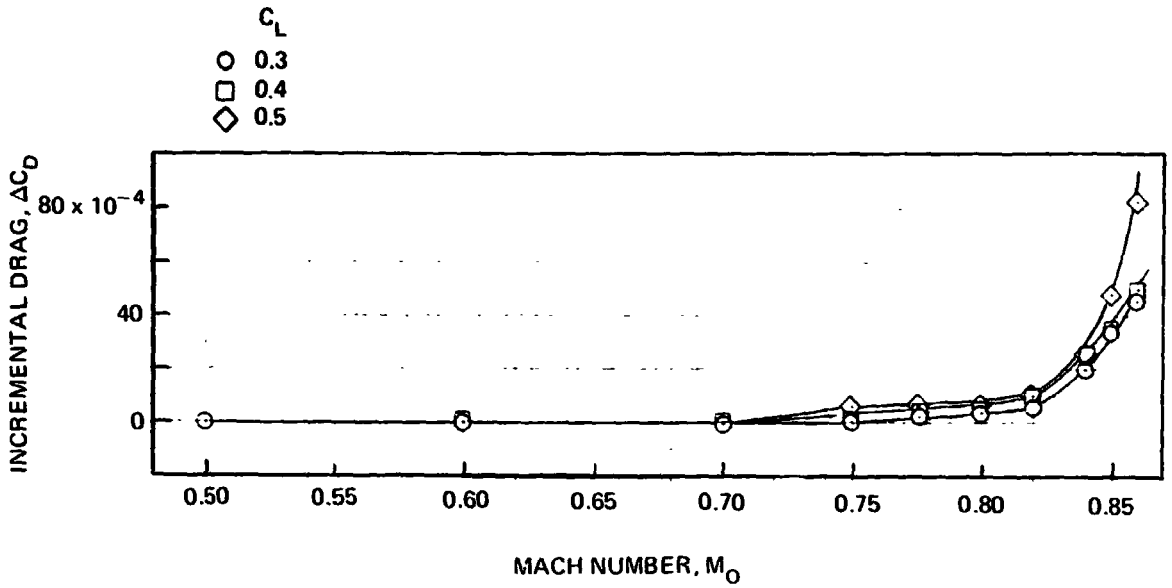

FIGURE 9. DRAG RISE OF WING-BODY MEASURED DURING PREVIOUS TEST IN AMES 11 FOOT TUNNEL

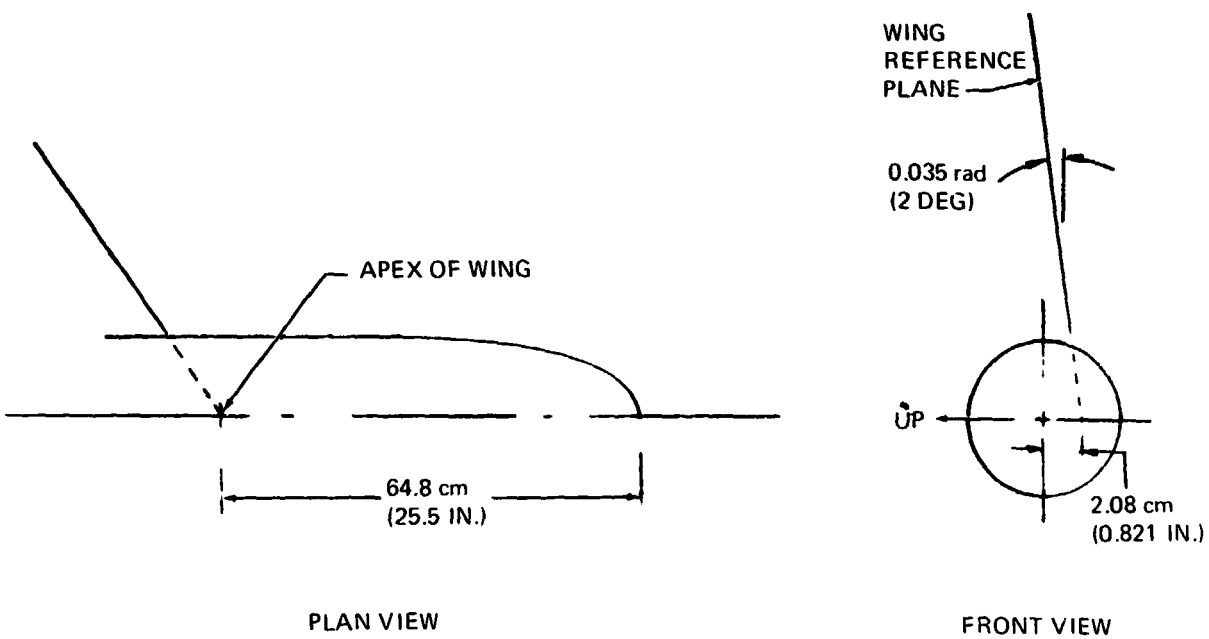

FIGURE 10. LOCATION OF WING REFERENCE PLANE

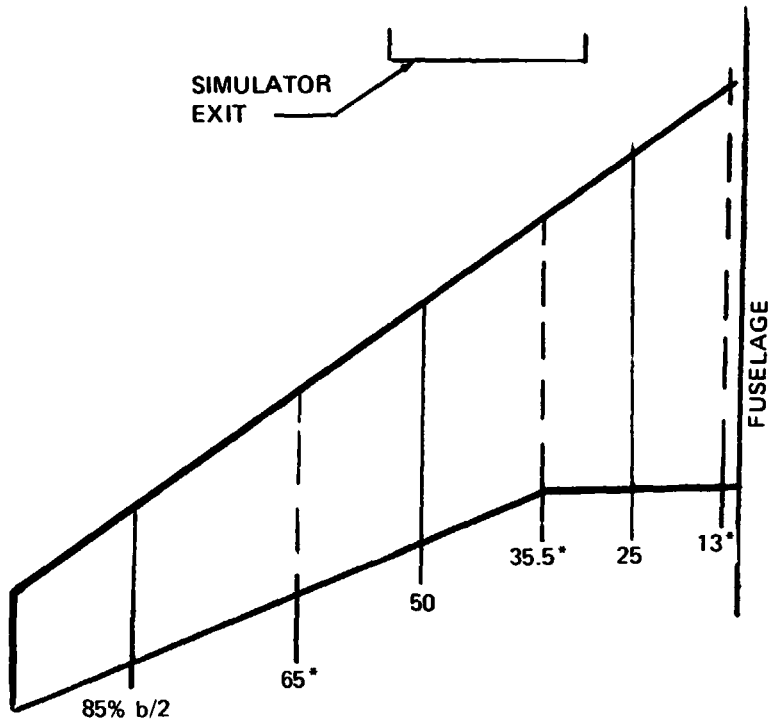

*LOCATED ON RIGHT HAND SIDE

FIGURE 11. LOCATION OF WING SURFACE PRESSURE

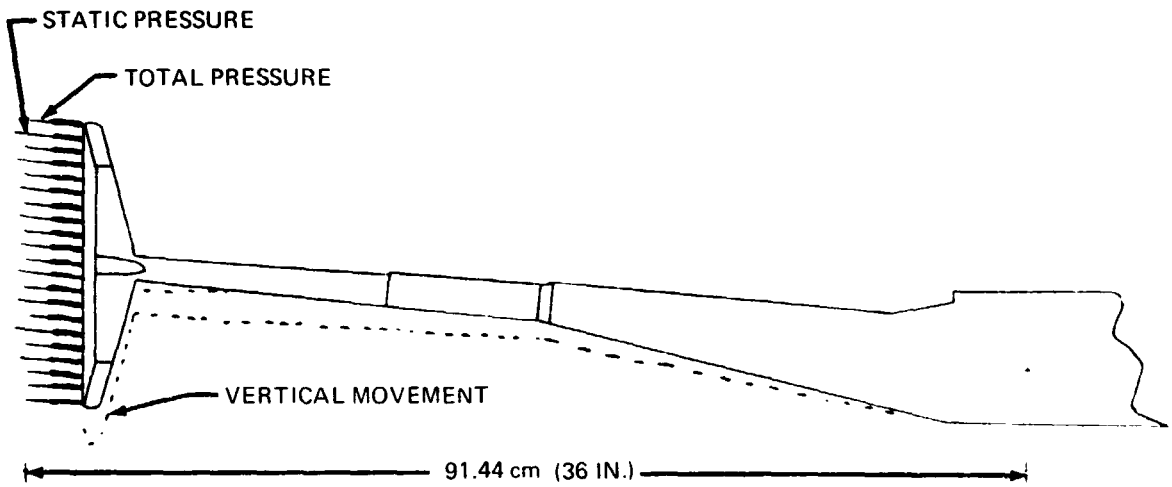

FIGURE 12. DESCRIPTION OF WAKE RAKE (SIDE VIEW)

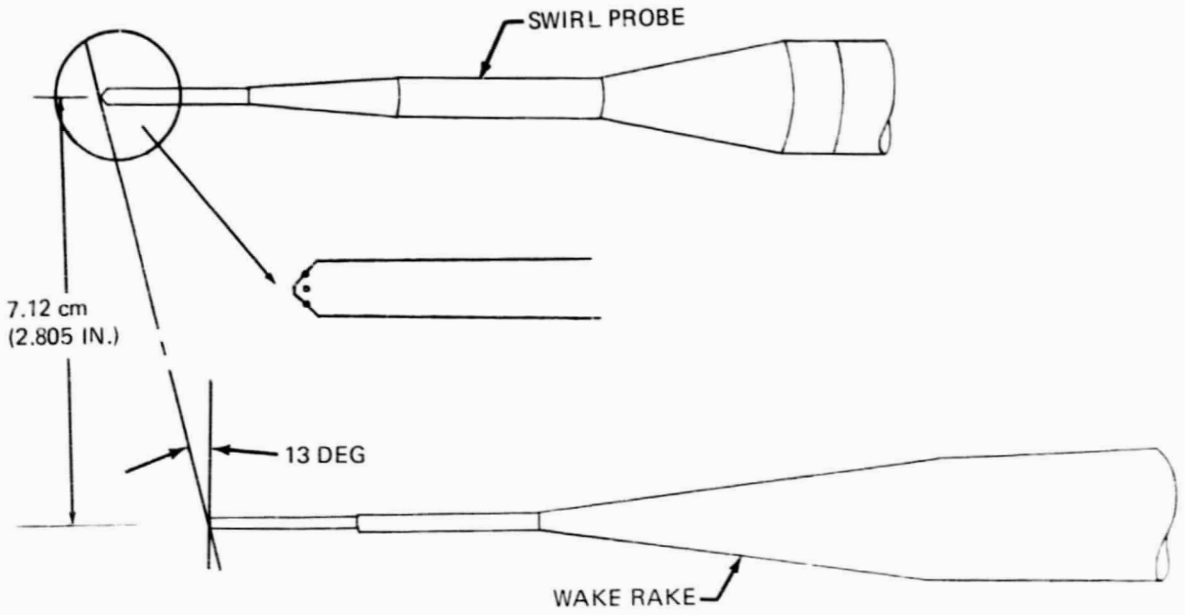

FIGURE 13. DESCRIPTION OF FLOW ANGLE PROBE (TOP VIEW)

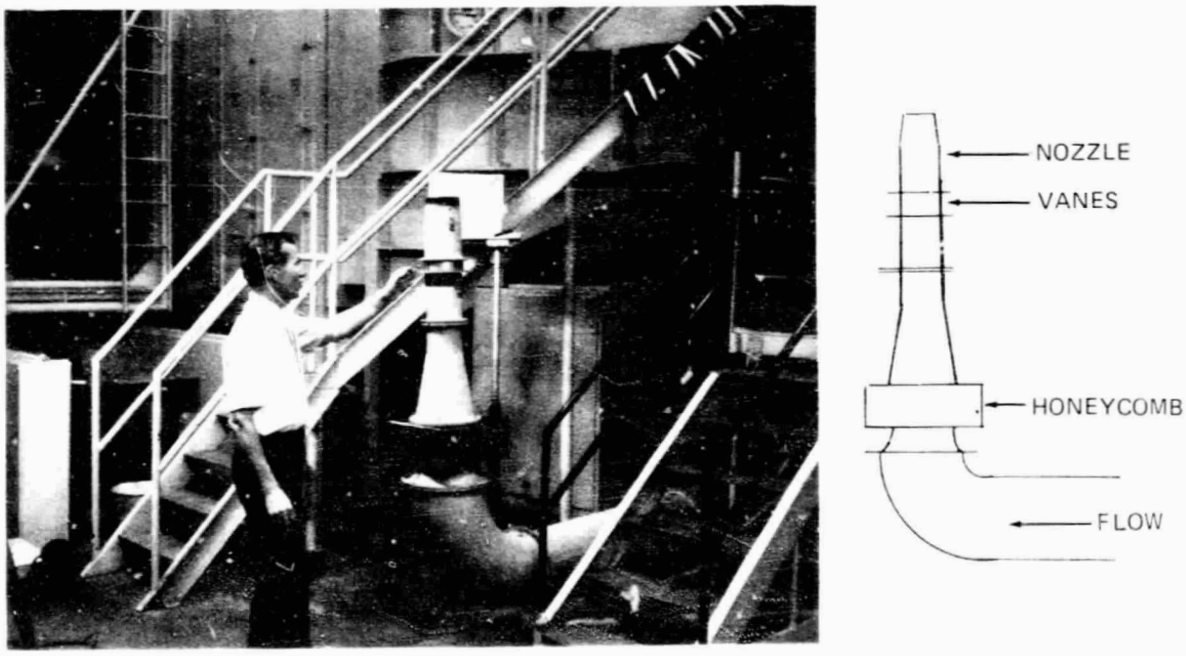

FIGURE 14. ILLUSTRATION OF SWIRL VANE FLOW TEST RIG

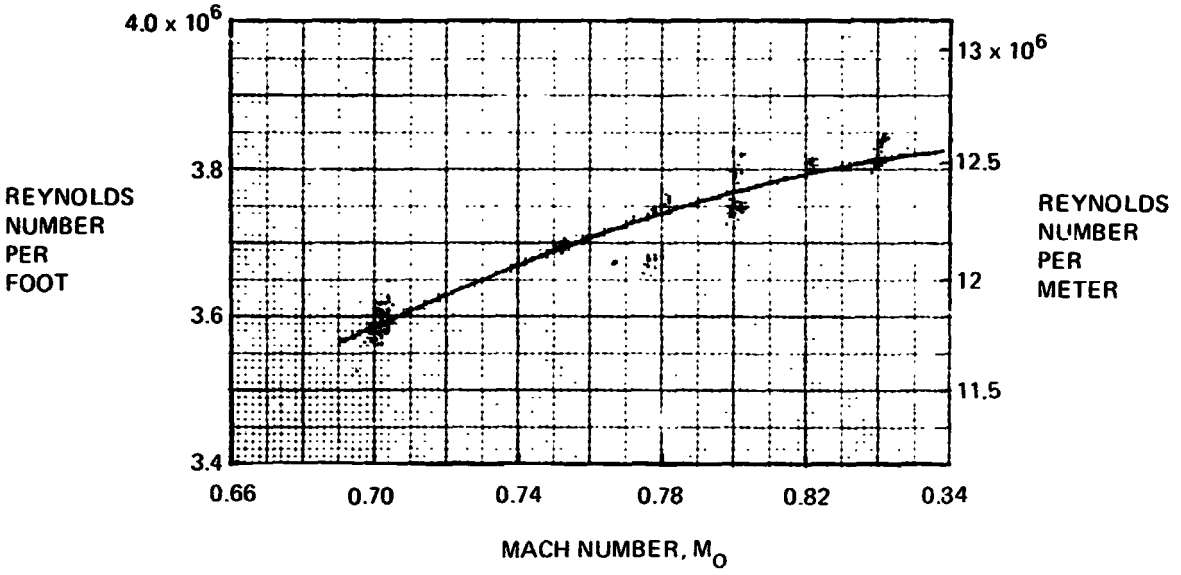

FIGURE 15. TEST REYNOLDS NUMBER VARIATION WITH MACH NUMBER

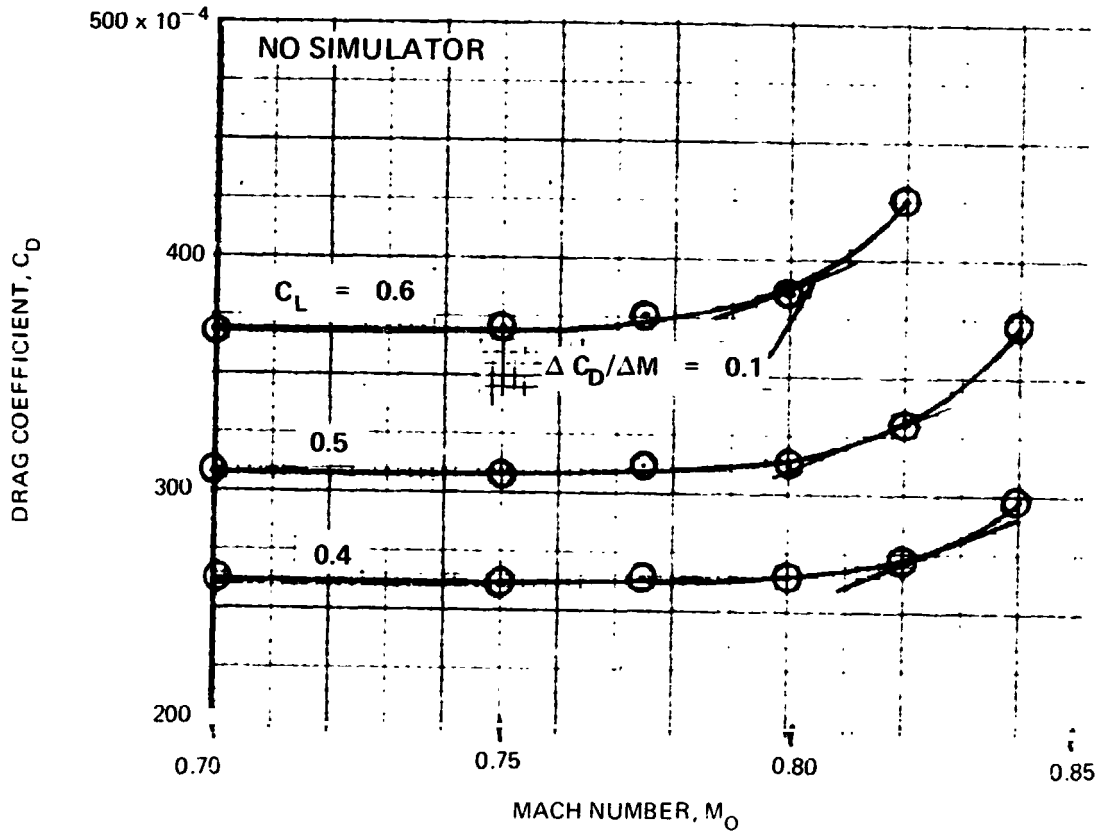

FIGURE 16. WING BODY ALONE – DRAG

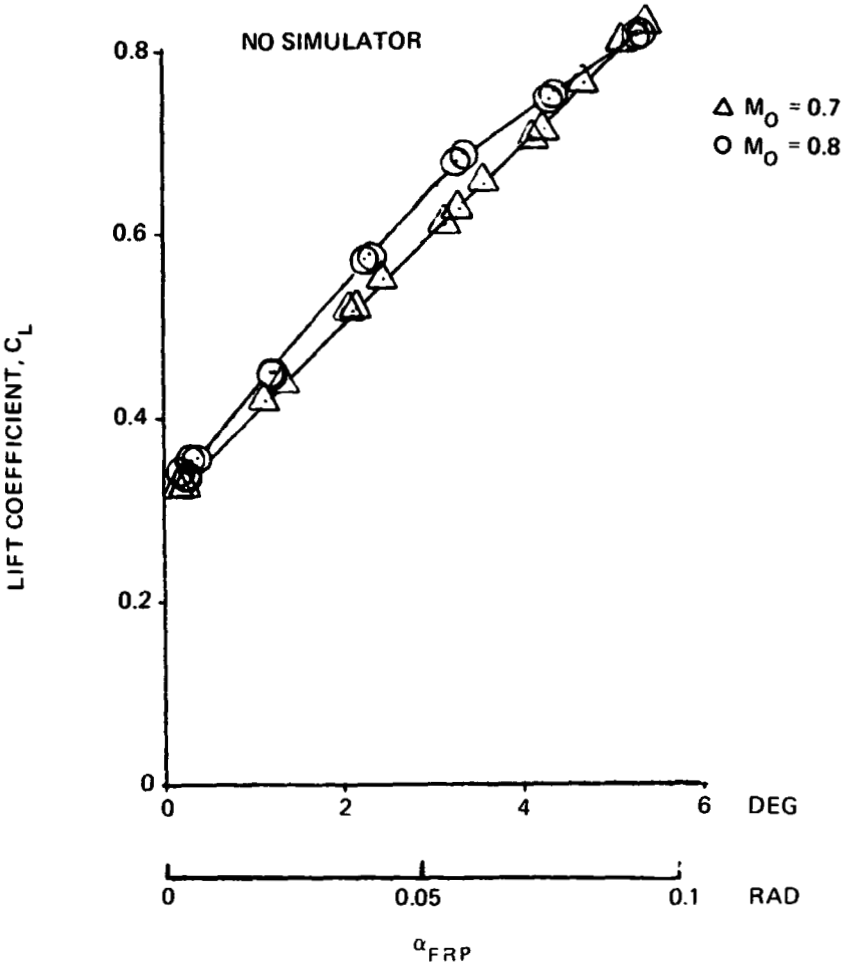

FIGURE 17. WING BODY ALONE – LIFT CURVE

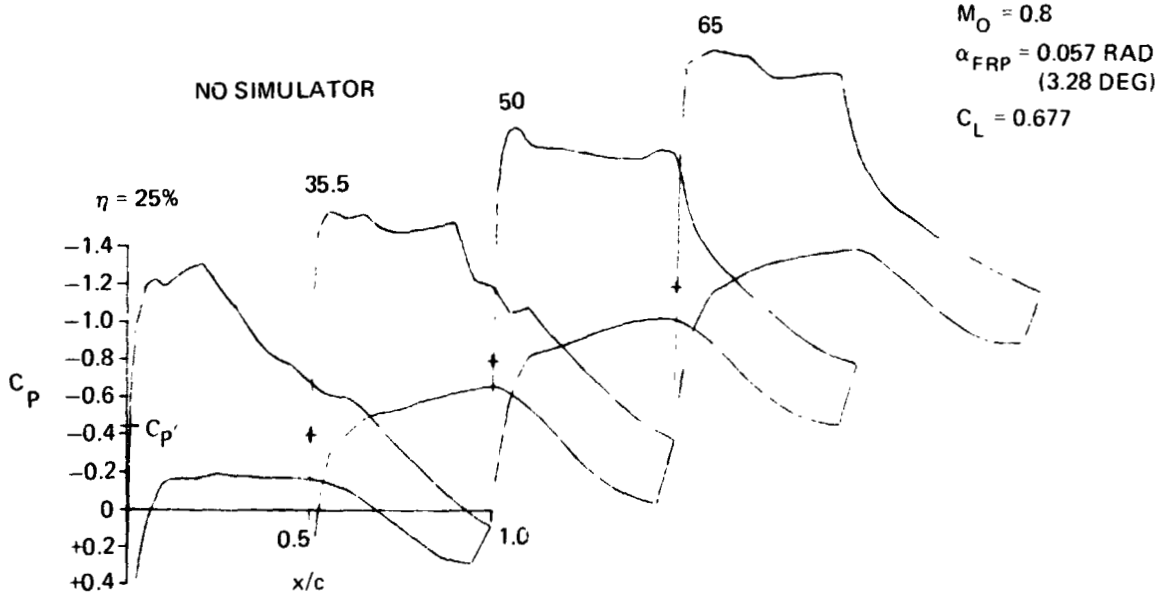

FIGURE 18. WING BODY ALONE – WING SURFACE PRESSURES

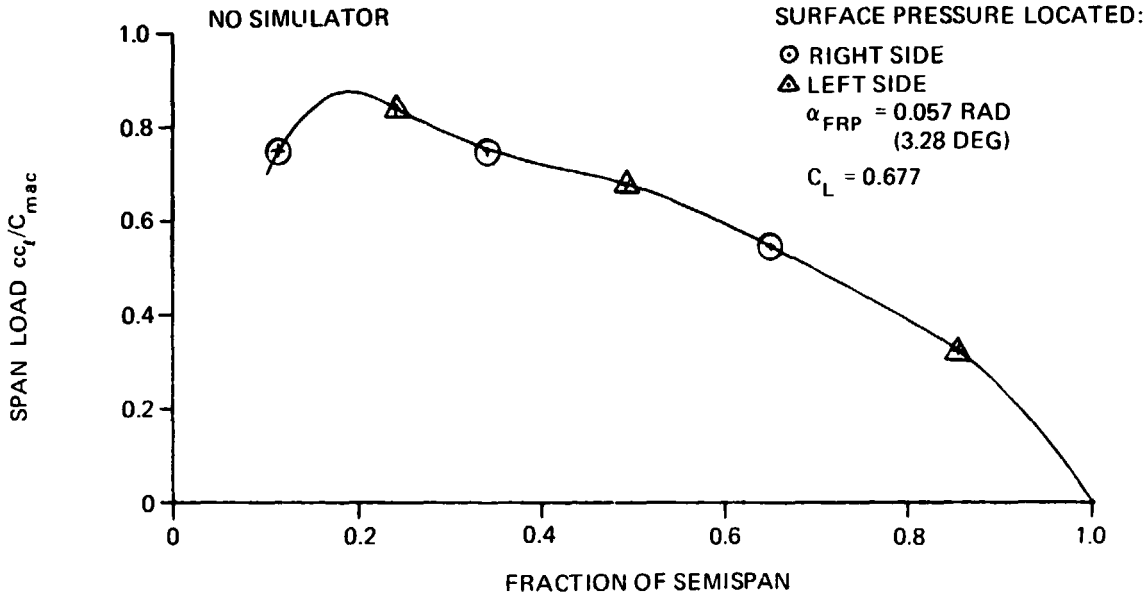

FIGURE 19. WING BODY ONLY SPAN LOADING AT M_0 = 0.8

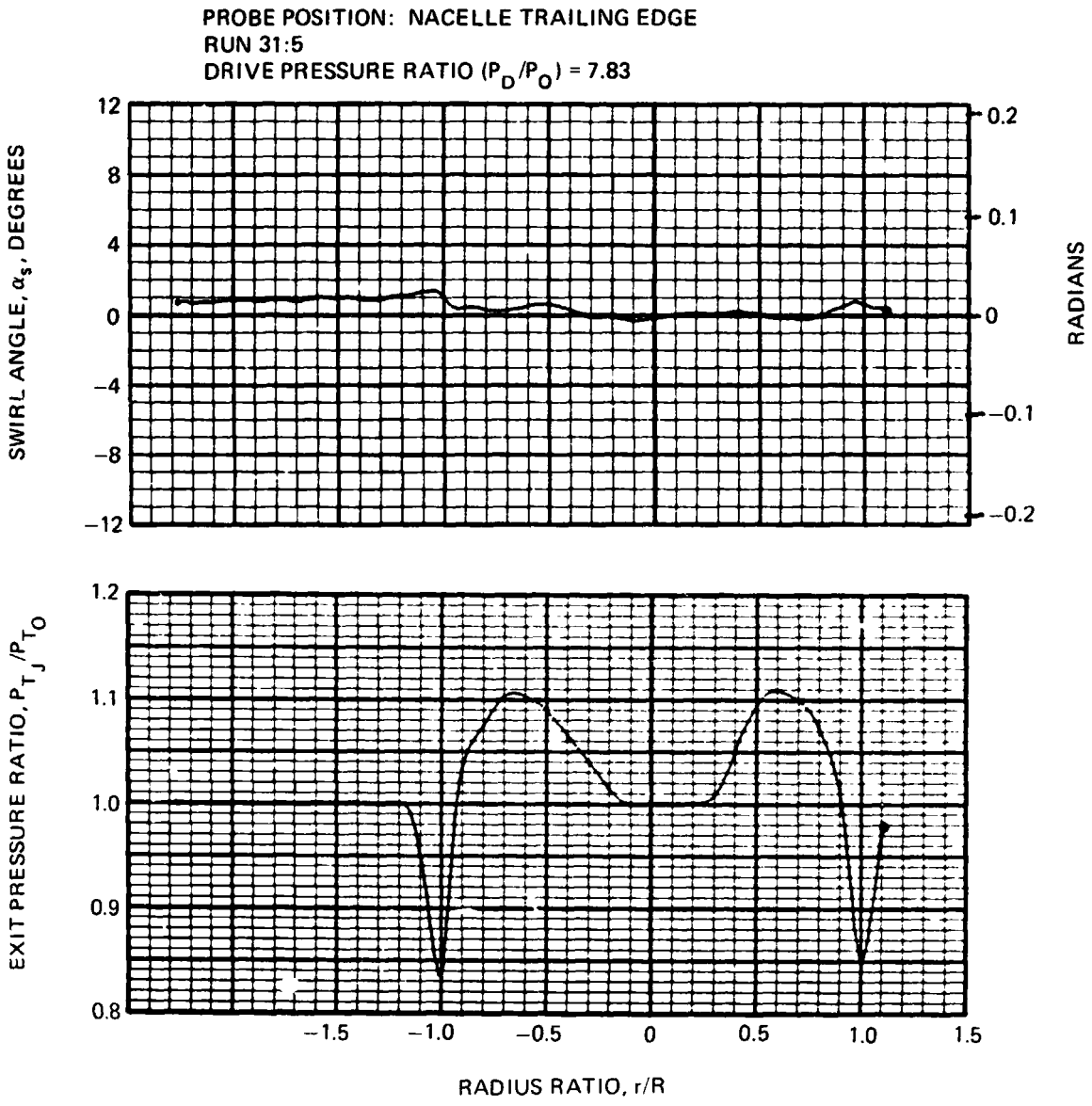

FIGURE 20. ZERO SWIRL SIMULATOR CALIBRATION AT M_0 = 0.8

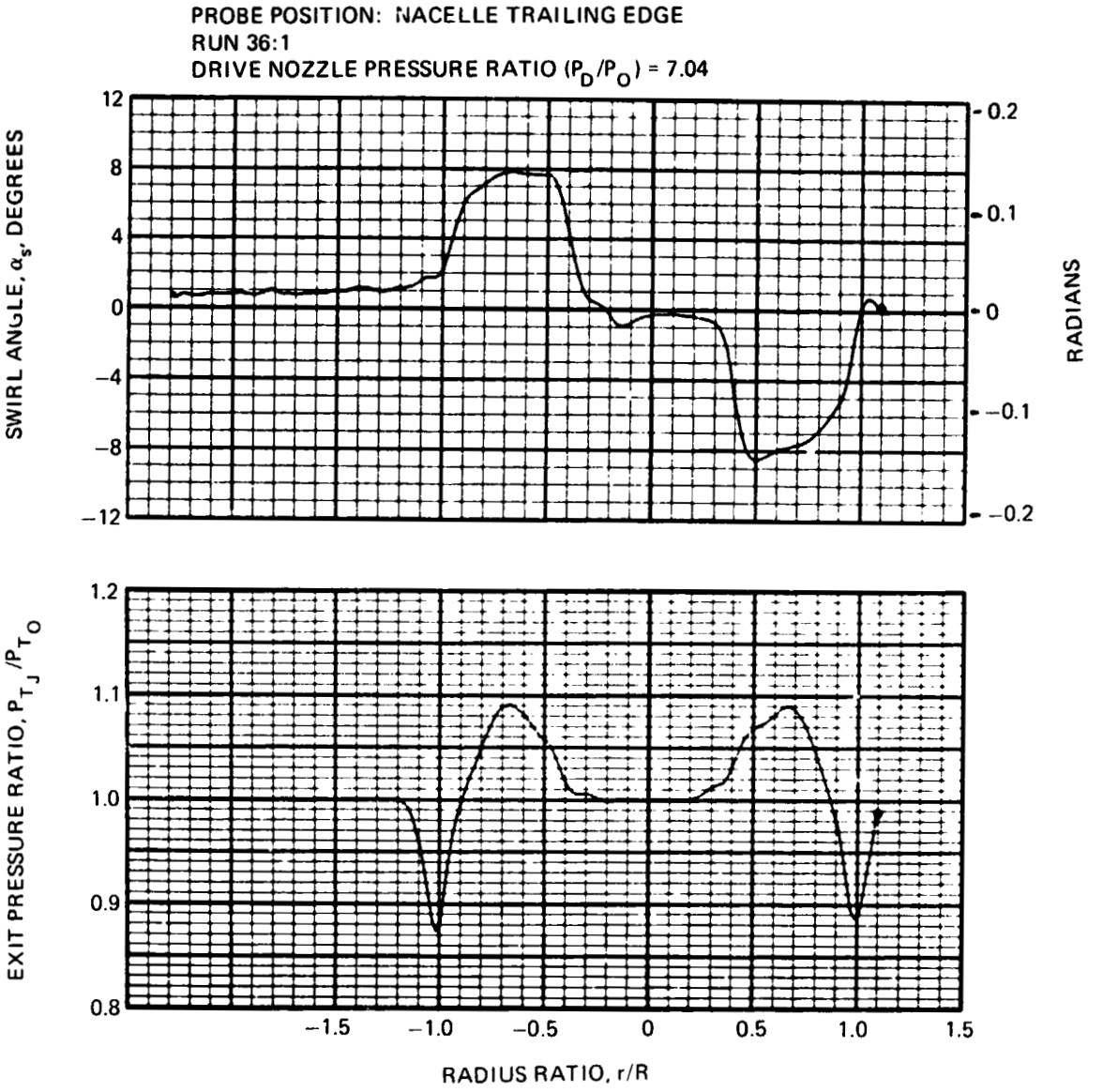

FIGURE 21. 0.105 RAD (6°) SWIRL (NOMINAL) CALIBRATION AT M_0 = 0.7

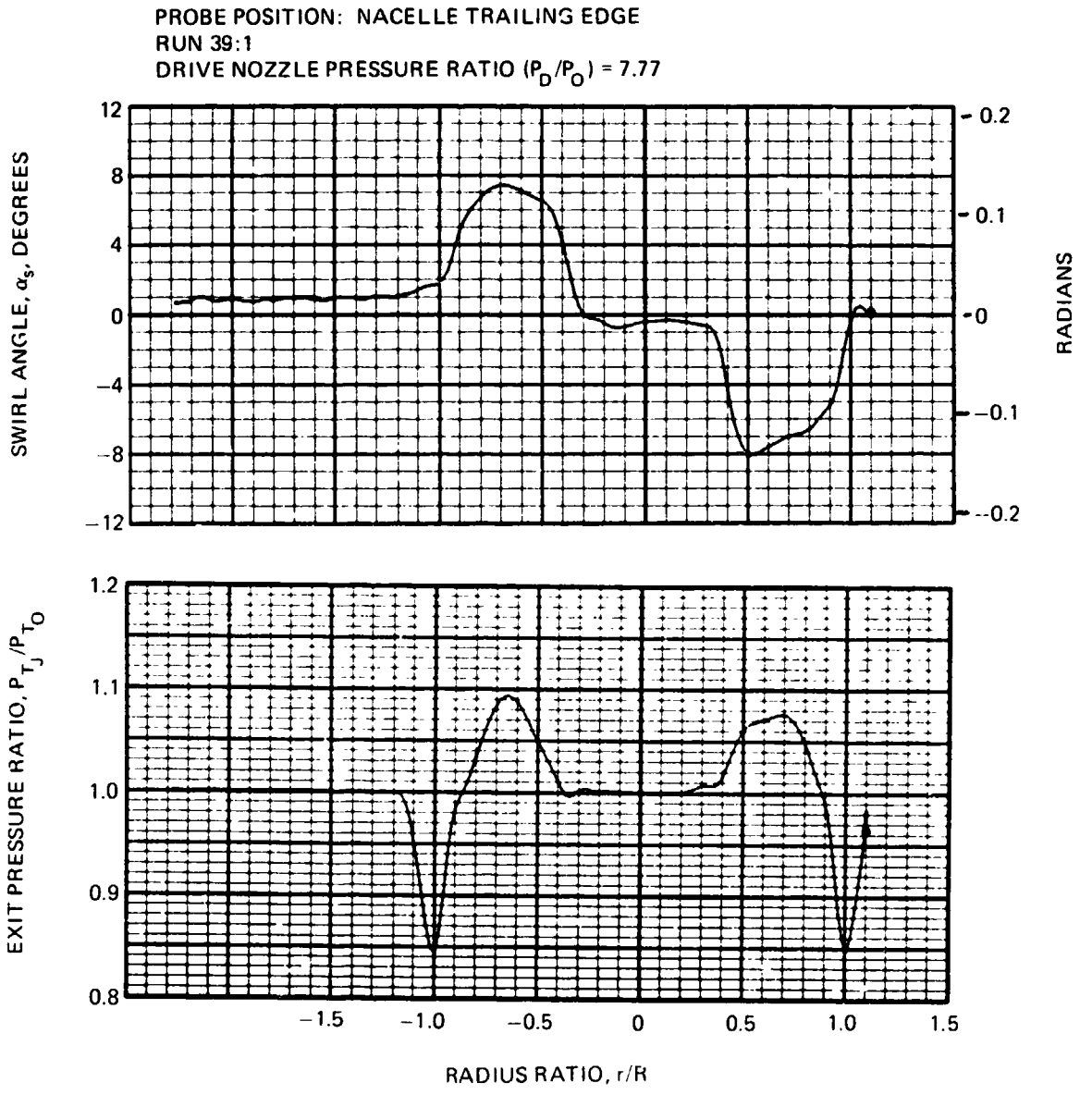

FIGURE 22. 0.105 RAD (6°) SWIRL (NOMINAL) CALIBRATION AT M_0 = 0.8

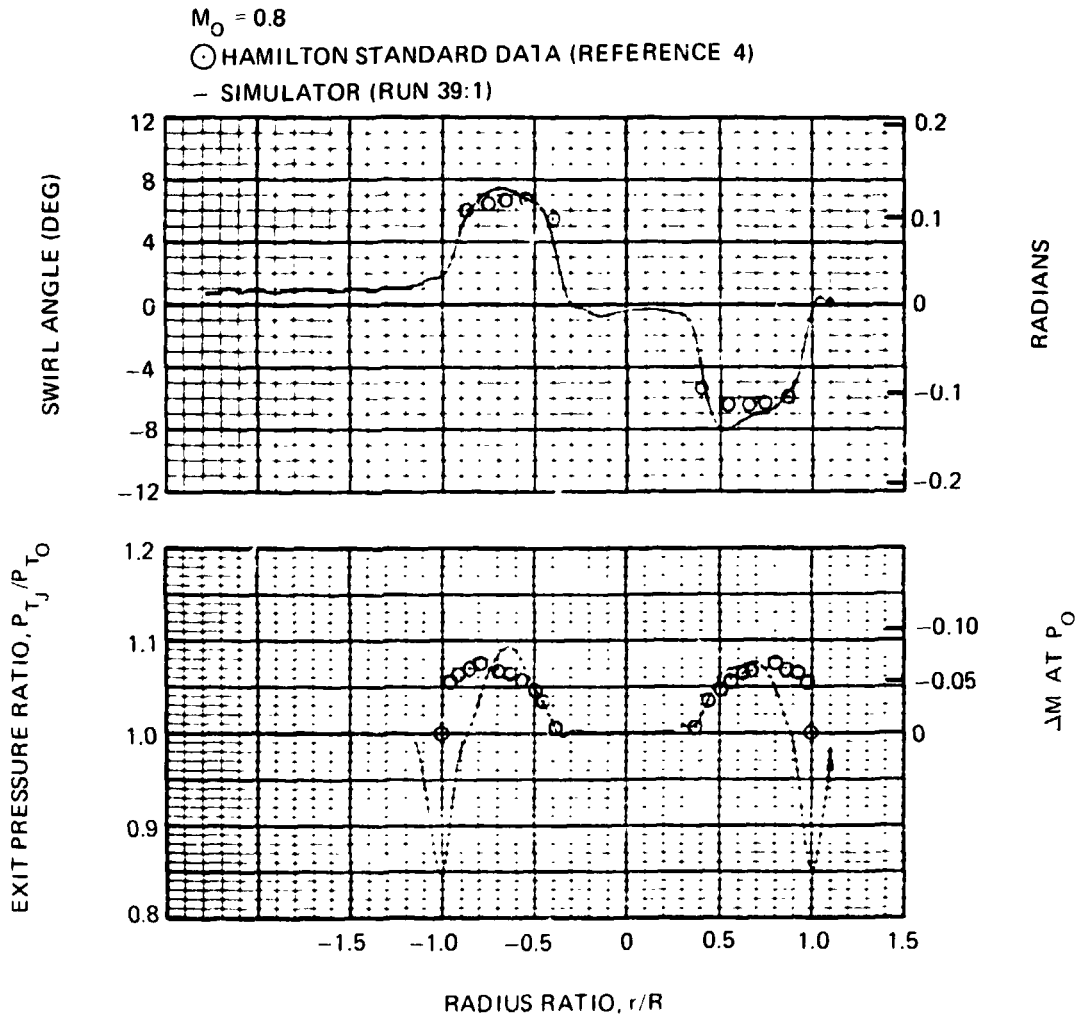

FIGURE 23. COMPARISON OF SIMULATOR EXIT FLOW WITH HAMILTON STANDARD PROPELLER DATA

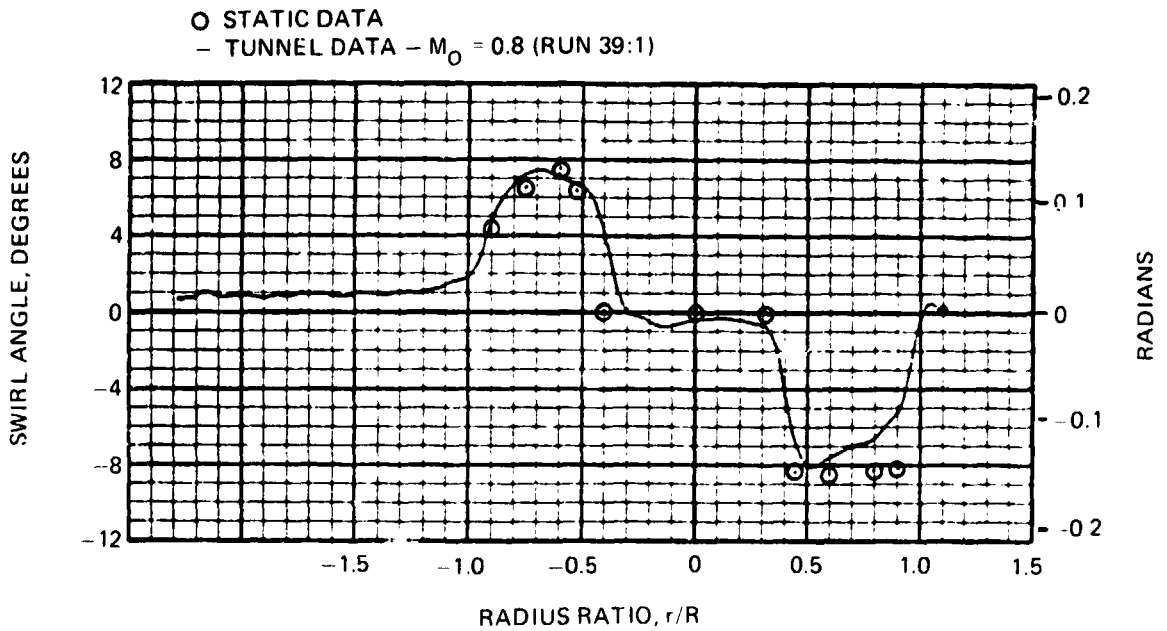

FIGURE 24. COMPARISON OF TUNNEL AND STATIC SWIRL ANGLE MEASUREMENTS FOR 0.105 RAD (6°) NOMINAL SWIRL VANE SET

PROBE POSITION*	RUN	P_D/P_O
—— NAC T.E.	39:2	5.38
---- WING C/4	55:1	4.99
××× WING T.E.	57.2	5.14

*WING NOT PRESENT – PROBE POSITION CORRESPONDS TO THESE LOCATIONS WHEN SIMULATOR AND WING ARE TESTED IN COMBINATION

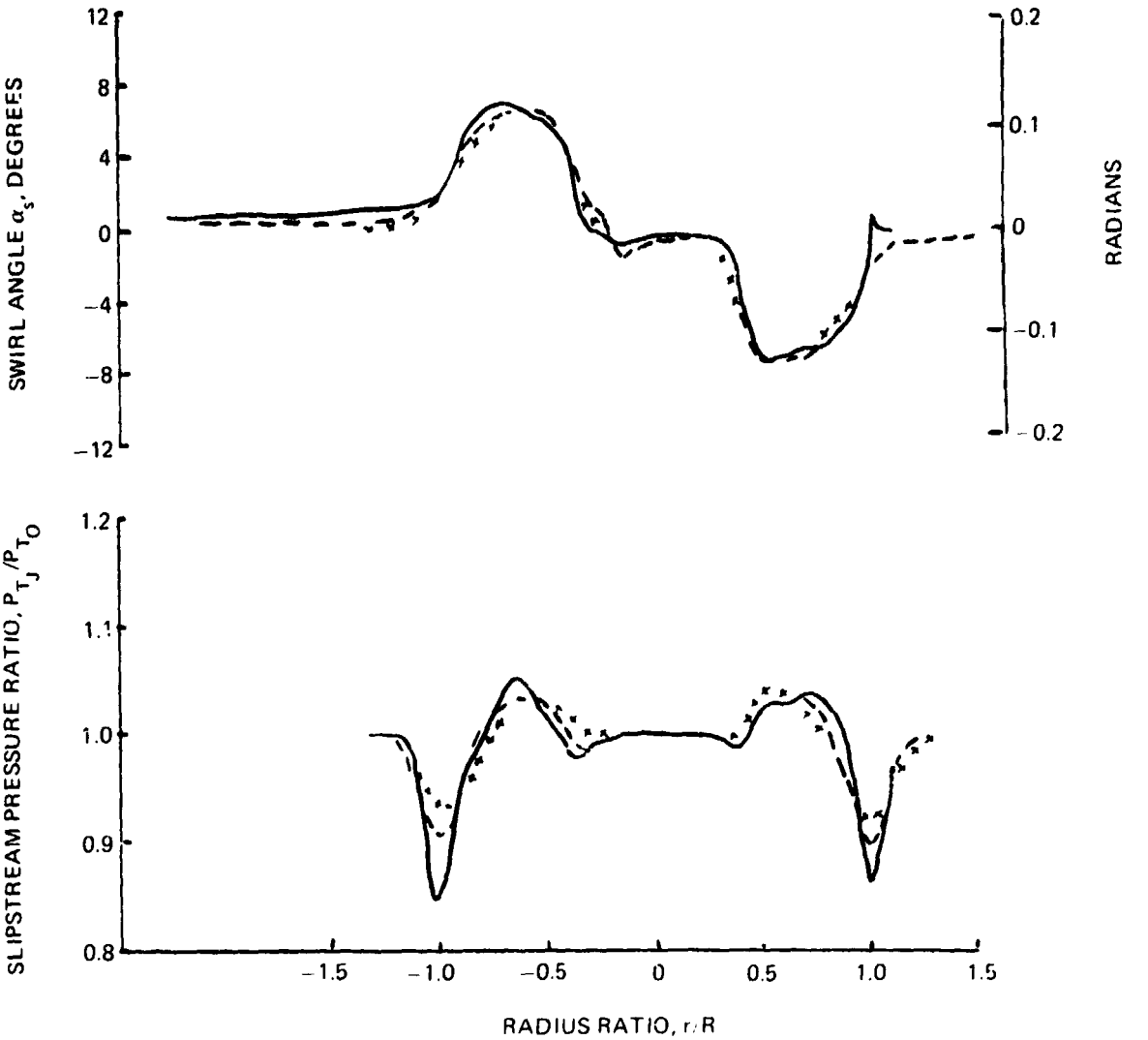

FIGURE 25. EFFECT OF STREAMWISE DISTANCE ON SLIPSTREAM PROFILES AT M_O = 0.8 AND 0.105 RAD (6°) NOMINAL SWIRL ANGLE

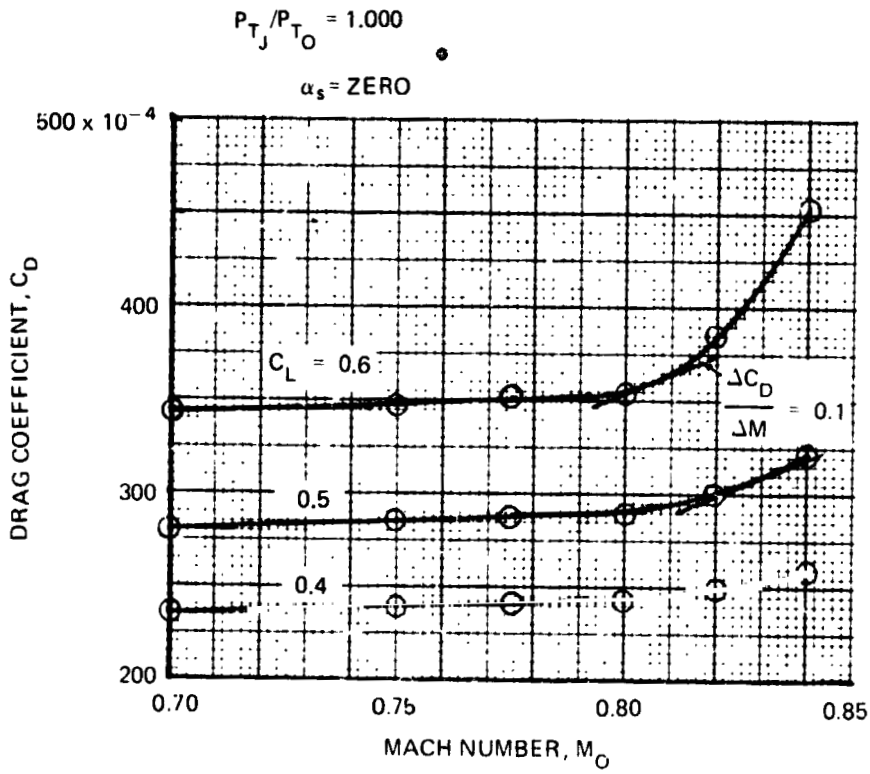

FIGURE 26. WING BODY DRAG AT SIMULATOR REFERENCE CONDITIONS

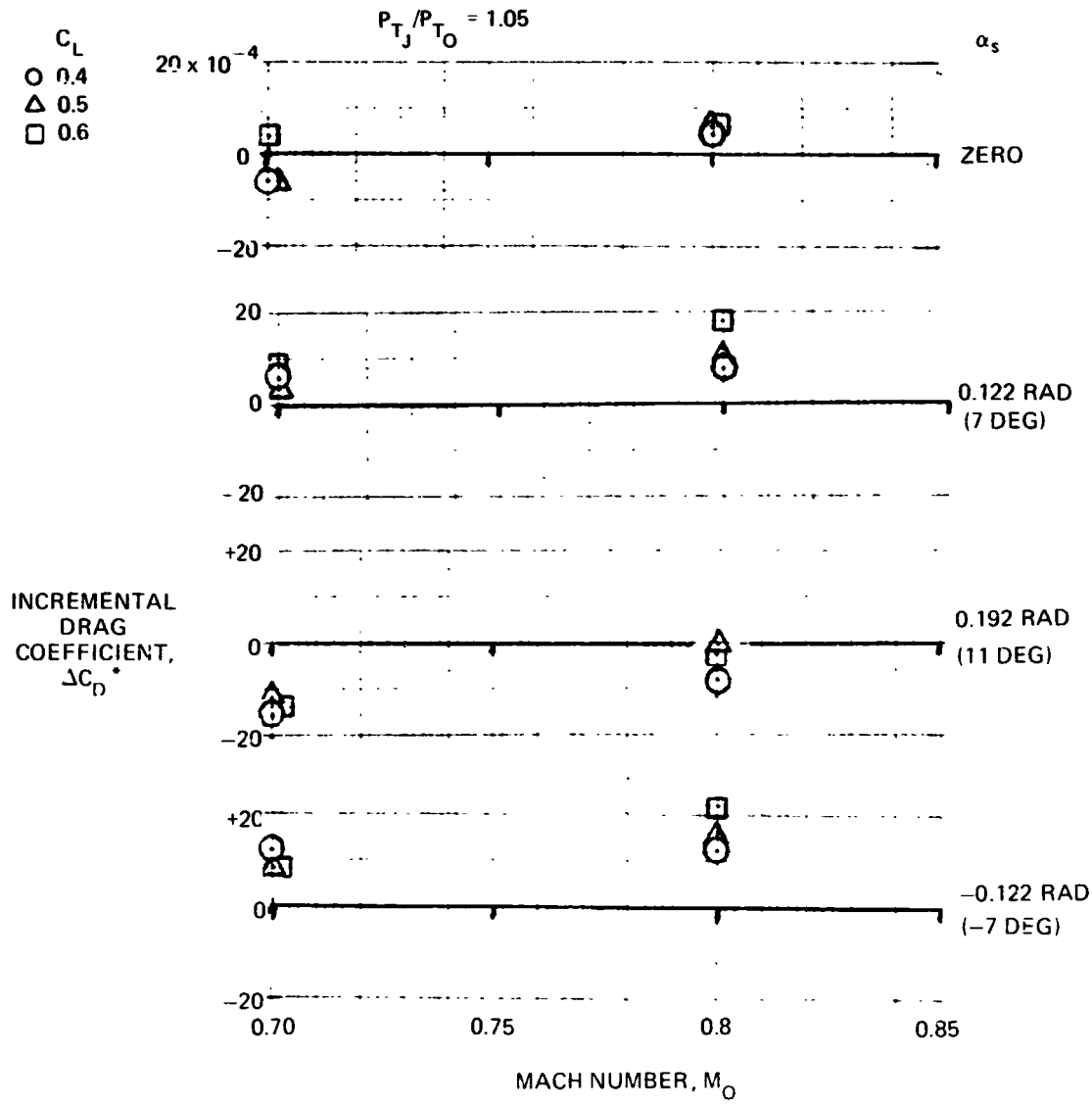

FIGURE 27. INCREMENTAL DRAG AT P_{T_J}/P_{T_0} = 1.05

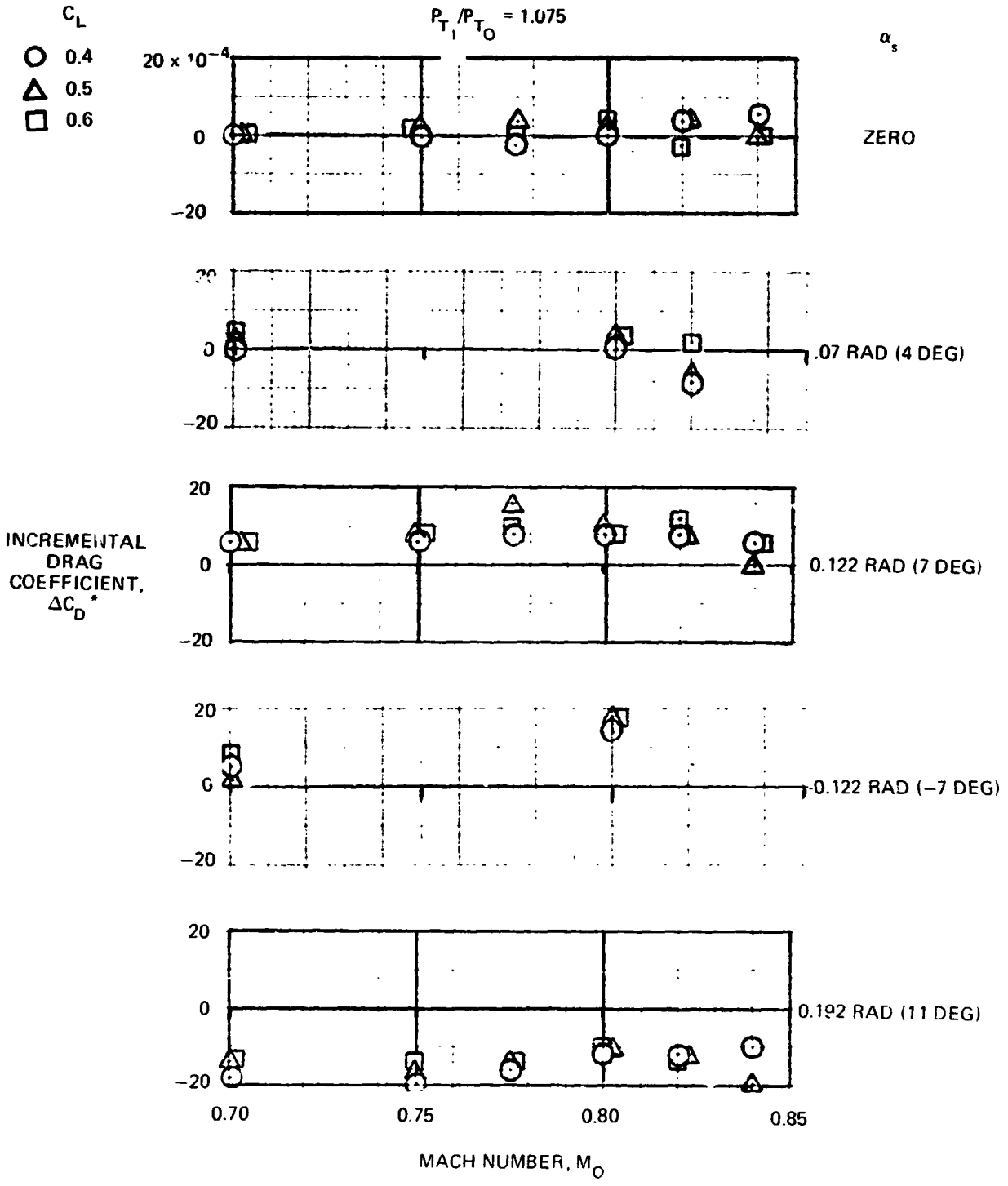

FIGURE 28. INCREMENTAL DRAG DATA AT P_{T_J}/P_{T_O} = 1.075

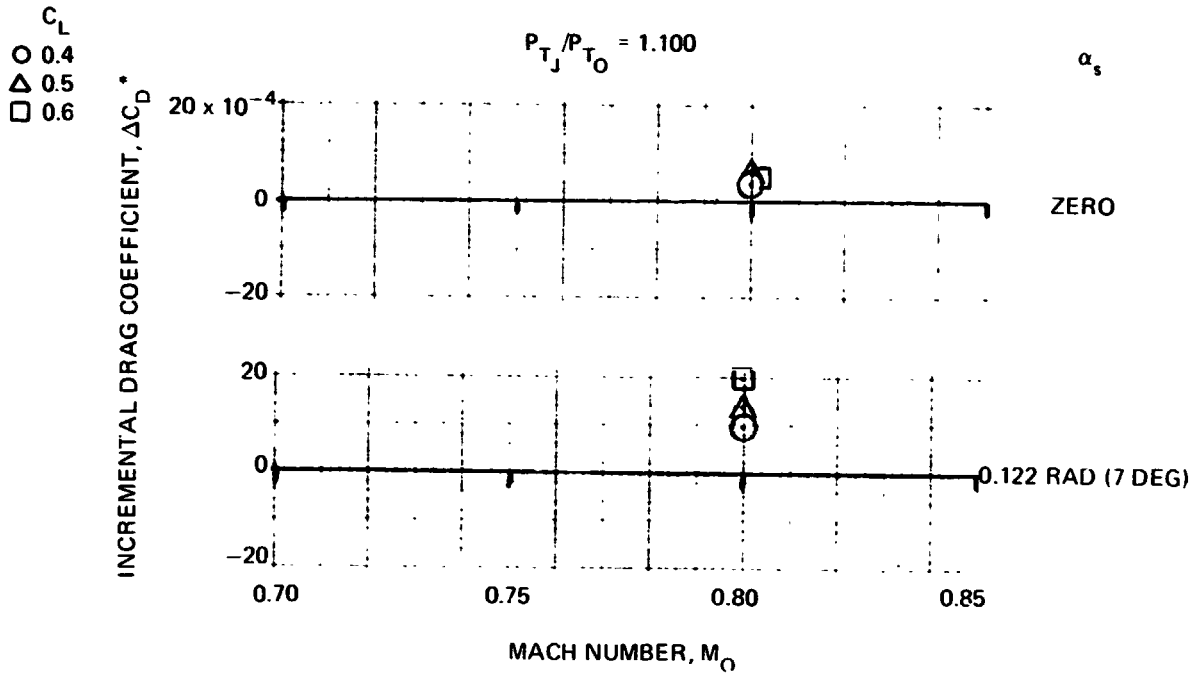

FIGURE 29. INCREMENTAL DRAG DATA AT P_{T_J}/P_{T_O} = 1.100

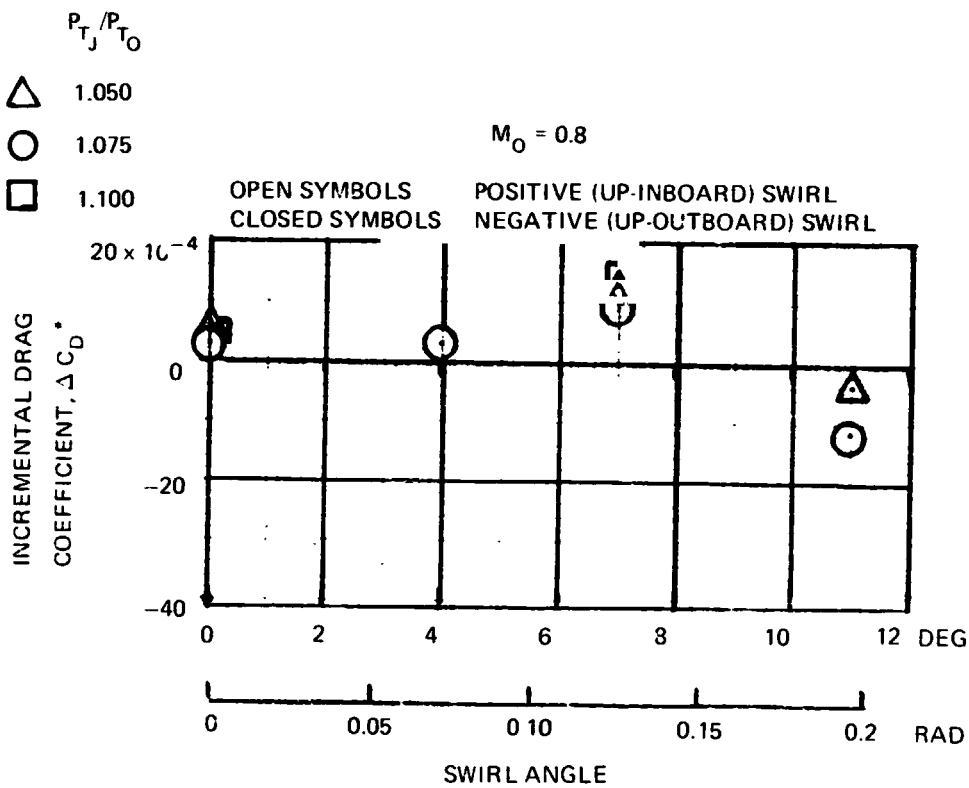

FIGURE 30. SUMMARY OF DRAG VARIATION WITH SWIRL ANGLE

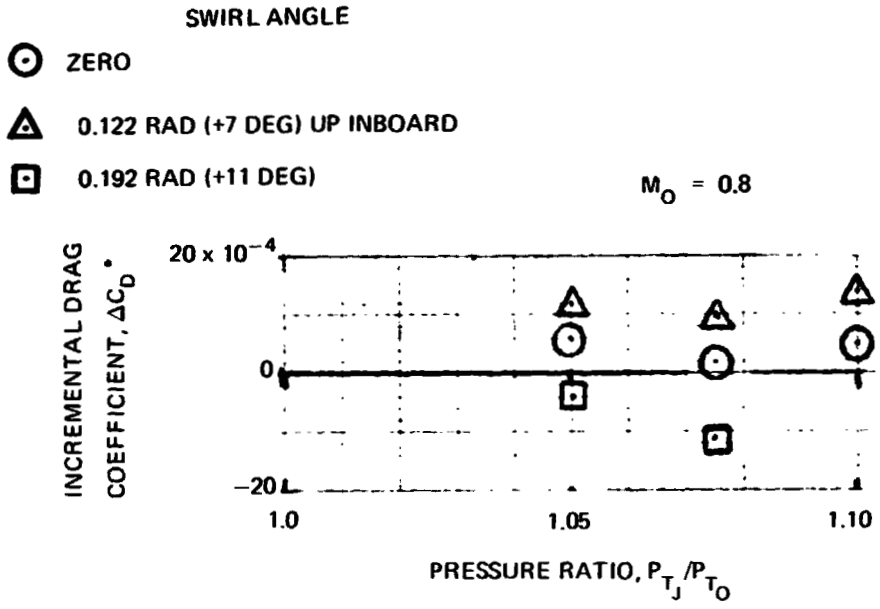

FIGURE 31. SUMMARY OF DRAG VARIATION WITH SIMULATED PROPELLER PRESSURE RATIO

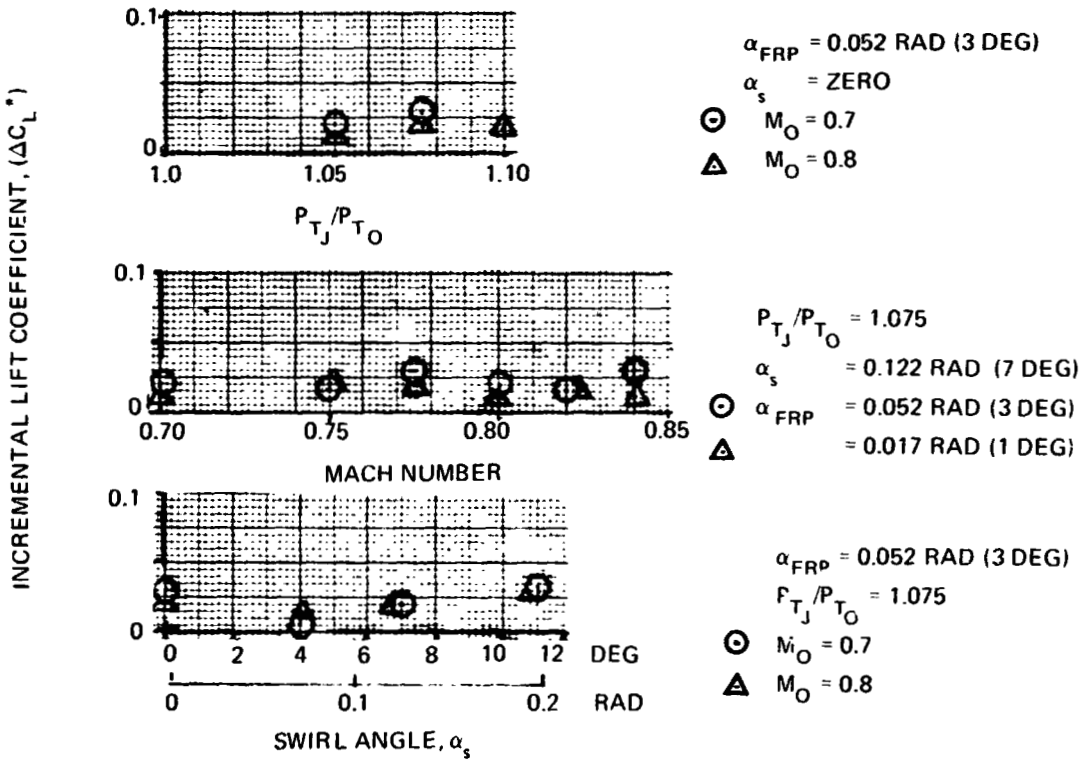

FIGURE 32. INCREMENTAL LIFT DATA

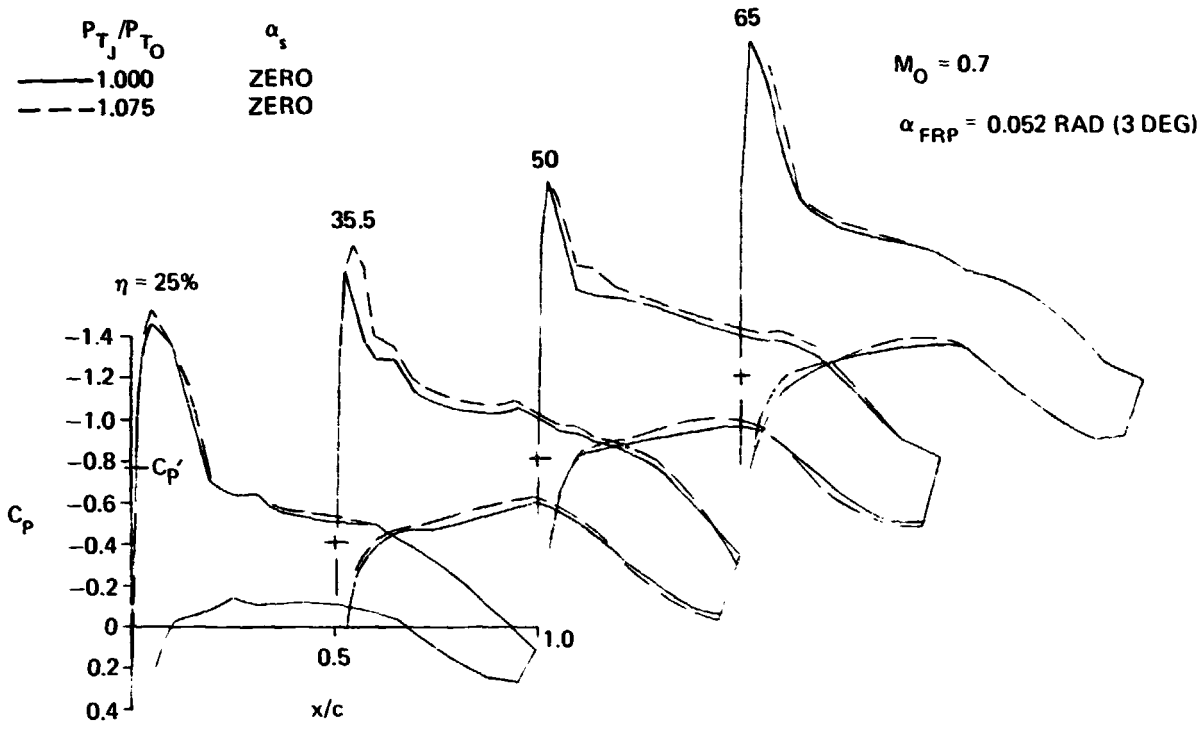

FIGURE 33. WING SURFACE PRESSURE VARIATION DUE TO POWER AT M_0 = 0.7

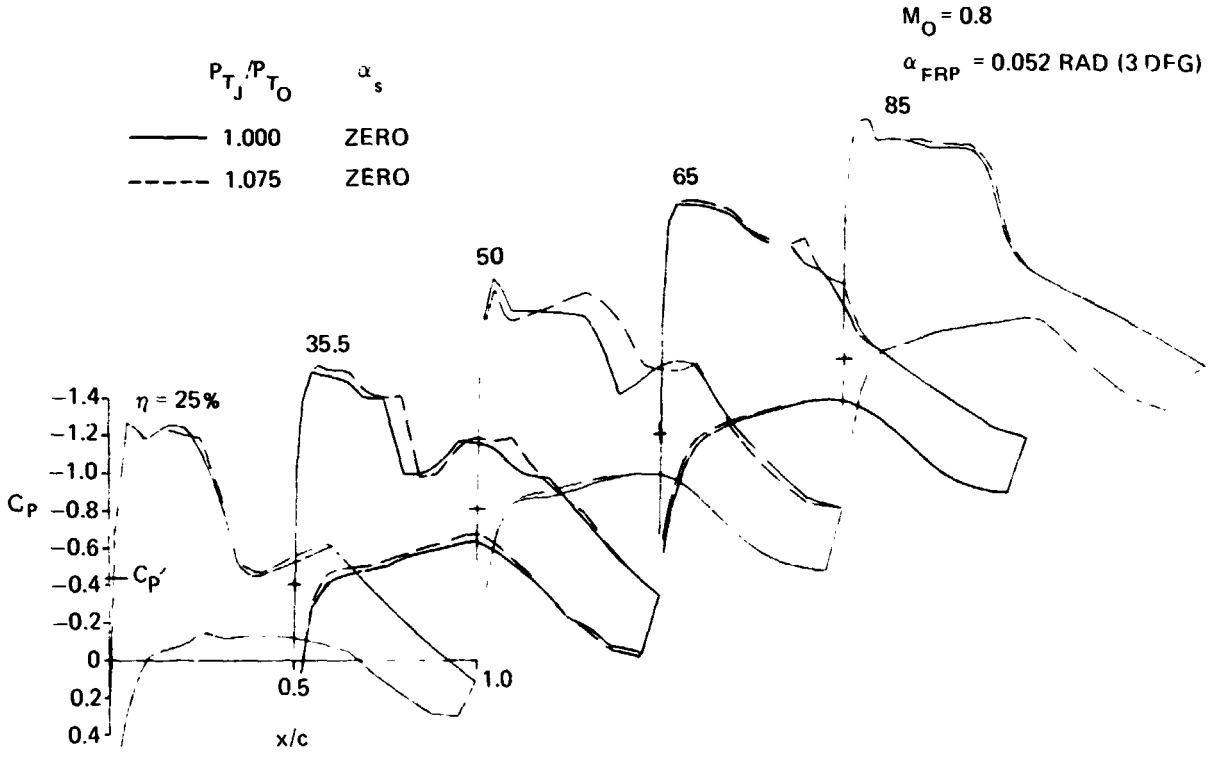

FIGURE 34. WING SURFACE PRESSURE VARIATION DUE TO POWER AT M_0 = 0.8

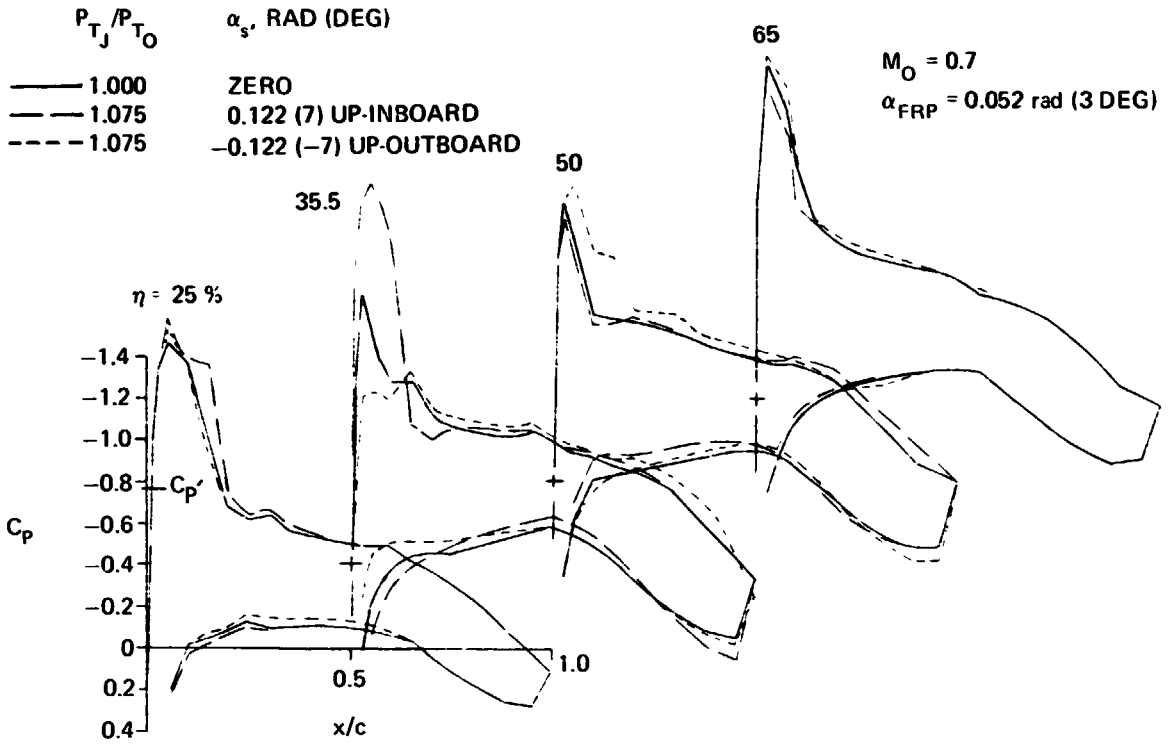

FIGURE 35. WING SURFACE PRESSURE VARIATION DUE TO POWER AND SWIRL AT M_0 = 0.7

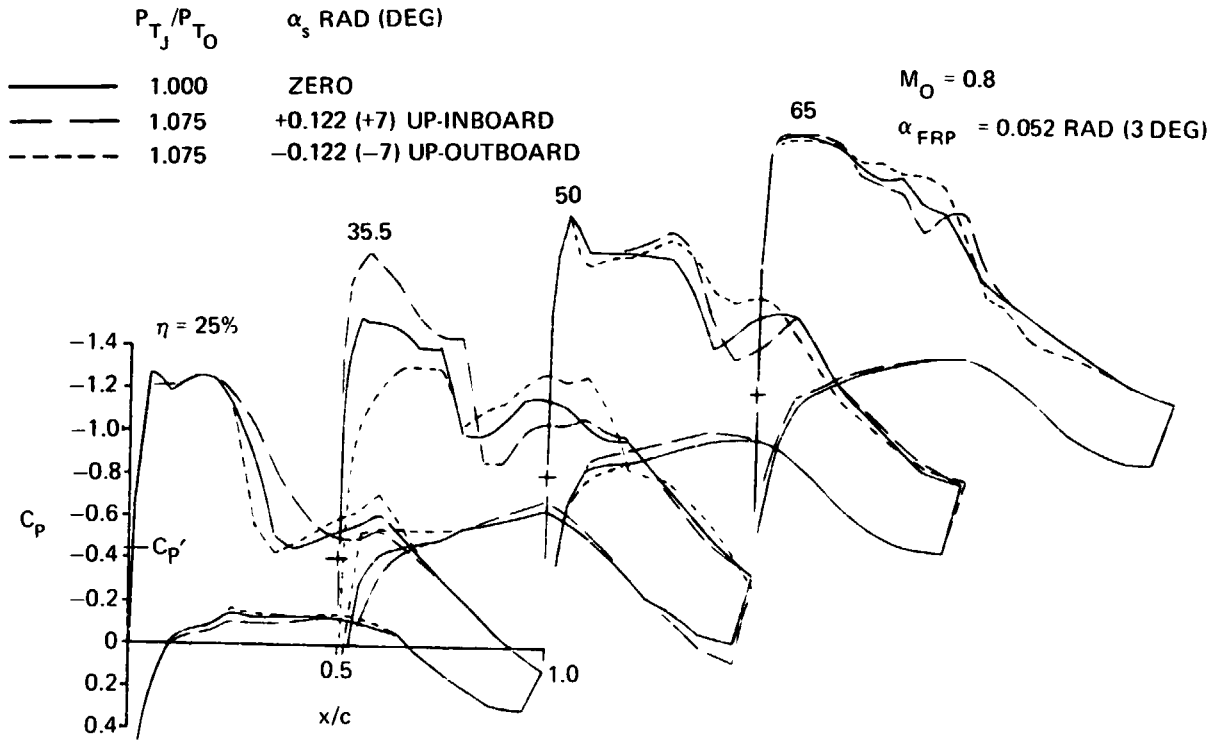

FIGURE 36. WING SURFACE PRESSURE VARIATION DUE TO POWER AND SWIRL AT M_0 = 0.8

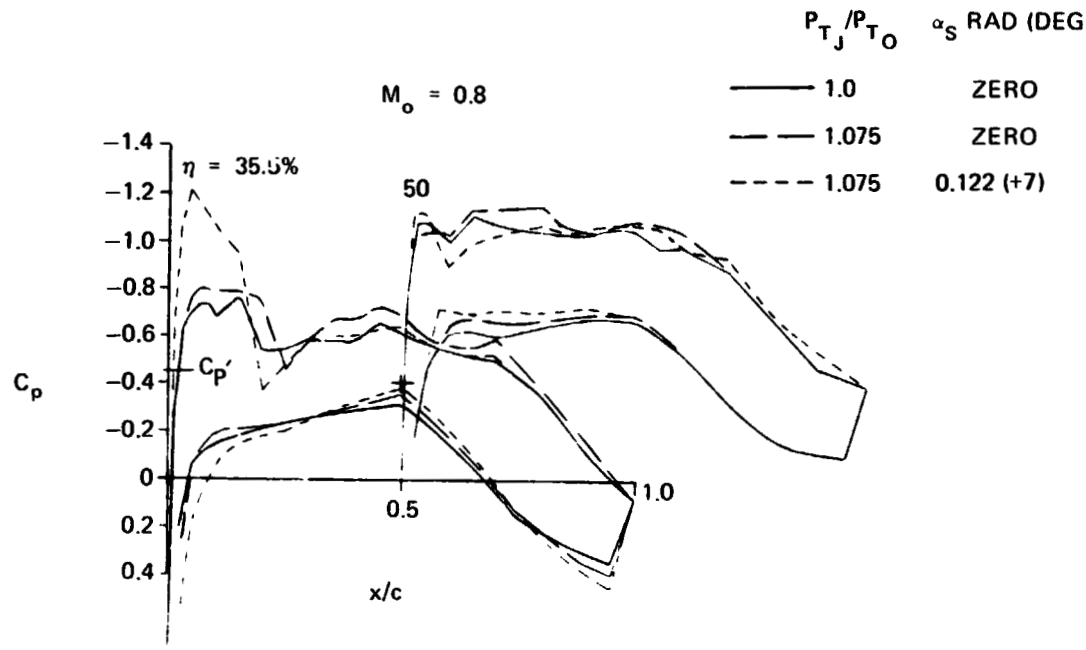

FIGURE 37. EFFECT OF POWER AND SWIRL AT α_{FRP} = 0.017 RAD (1 DEG)

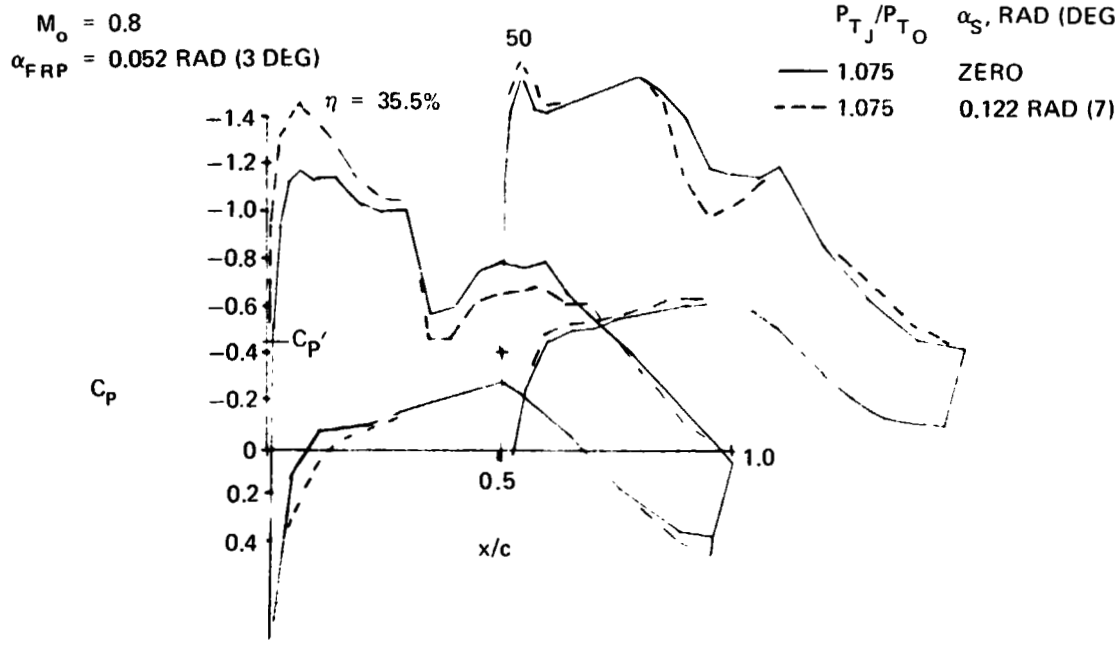

FIGURE 38. WING SURFACE PRESSURE VARIATION DUE TO 0.122 RAD (7 DEG) OF SWIRL

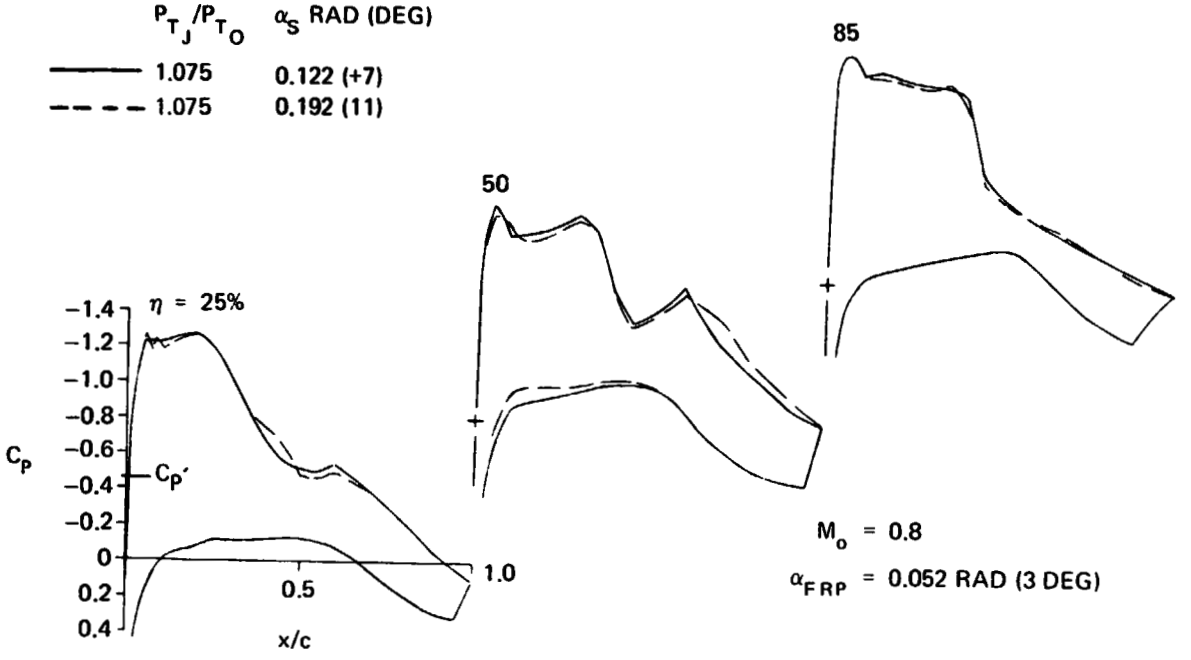

FIGURE 39. EFFECT OF 0.192 RAD (11 DEG) SWIRL ON WING SURFACE PRESSURES

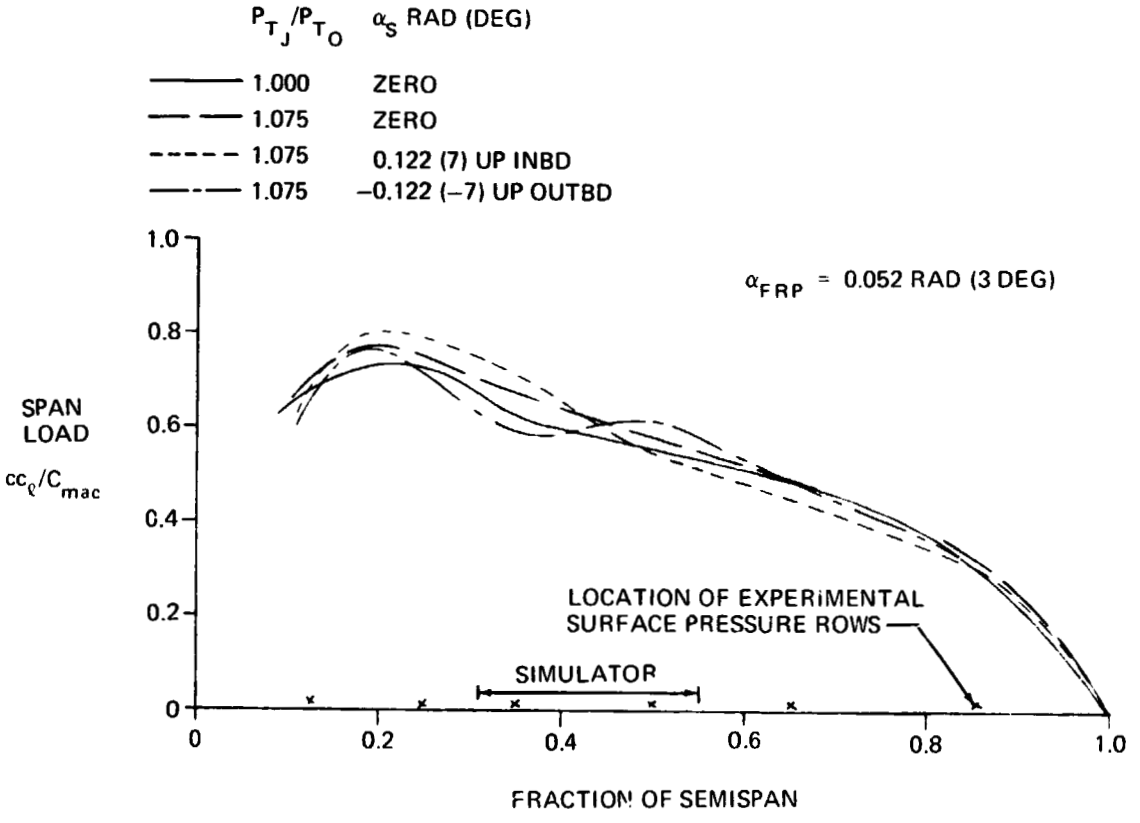

FIGURE 40. SPAN LOADING AT M_0 = 0.7

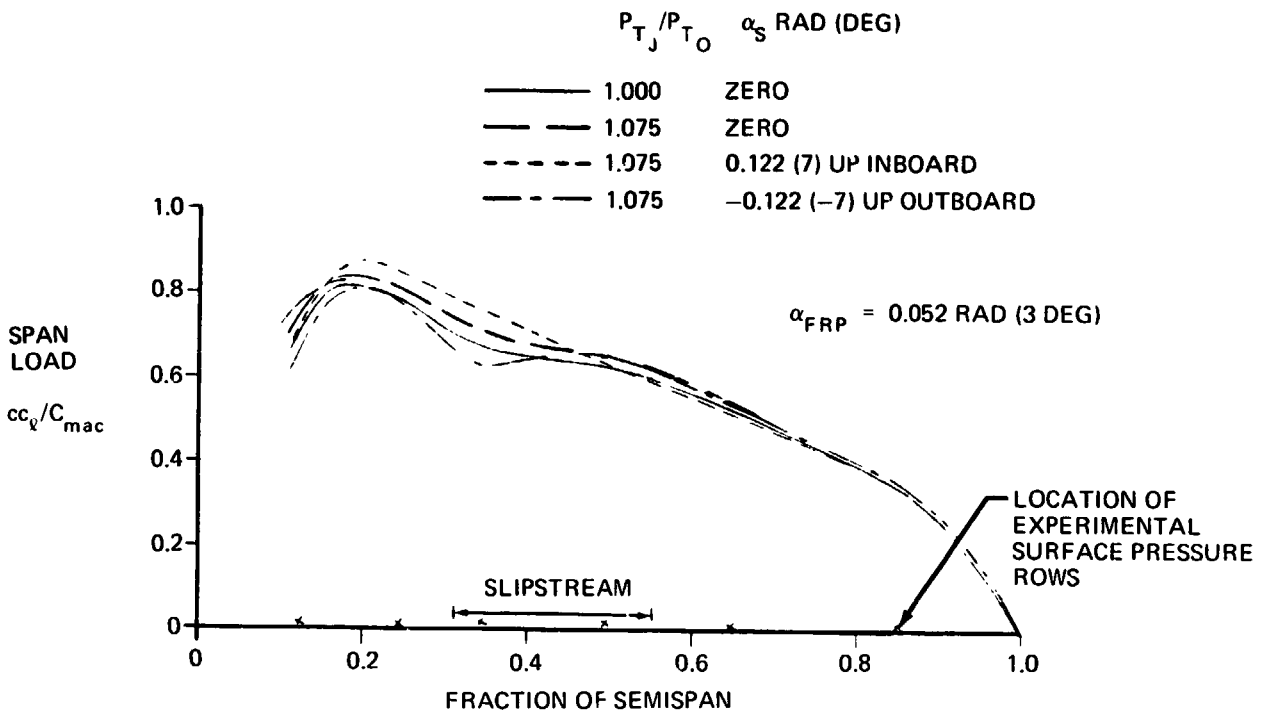

FIGURE 41. SPAN LOADING AT M_0 = 0.8

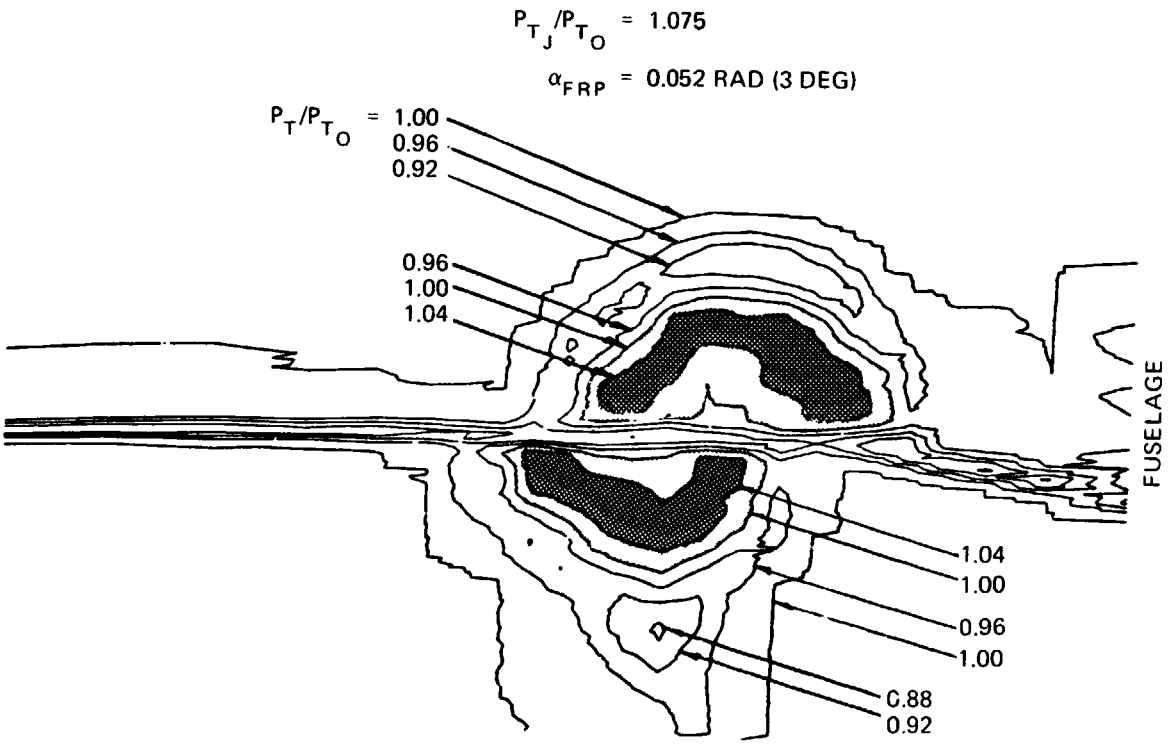

FIGURE 42. WAKE RAKE SURVEY AT M_0 = 0.8 WITH ZERO SWIRL

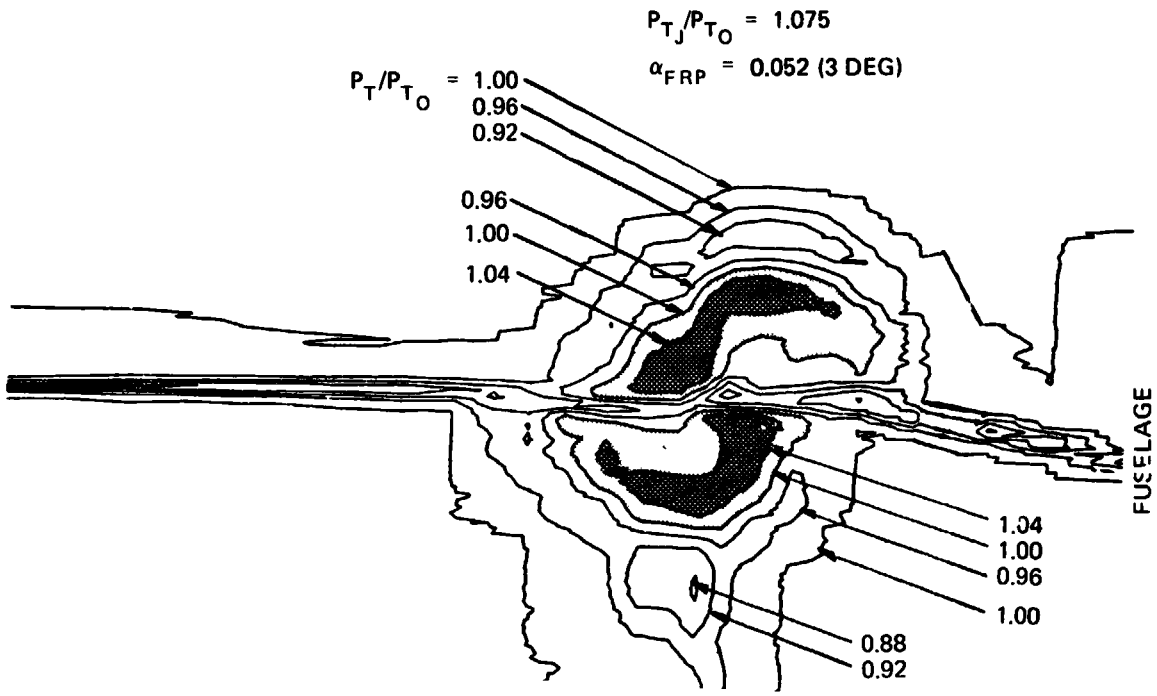

FIGURE 43. WAKE RAKE SURVEY AT M_0 = 0.8 AND 0.122 RAD (7 DEG) OF SWIRL

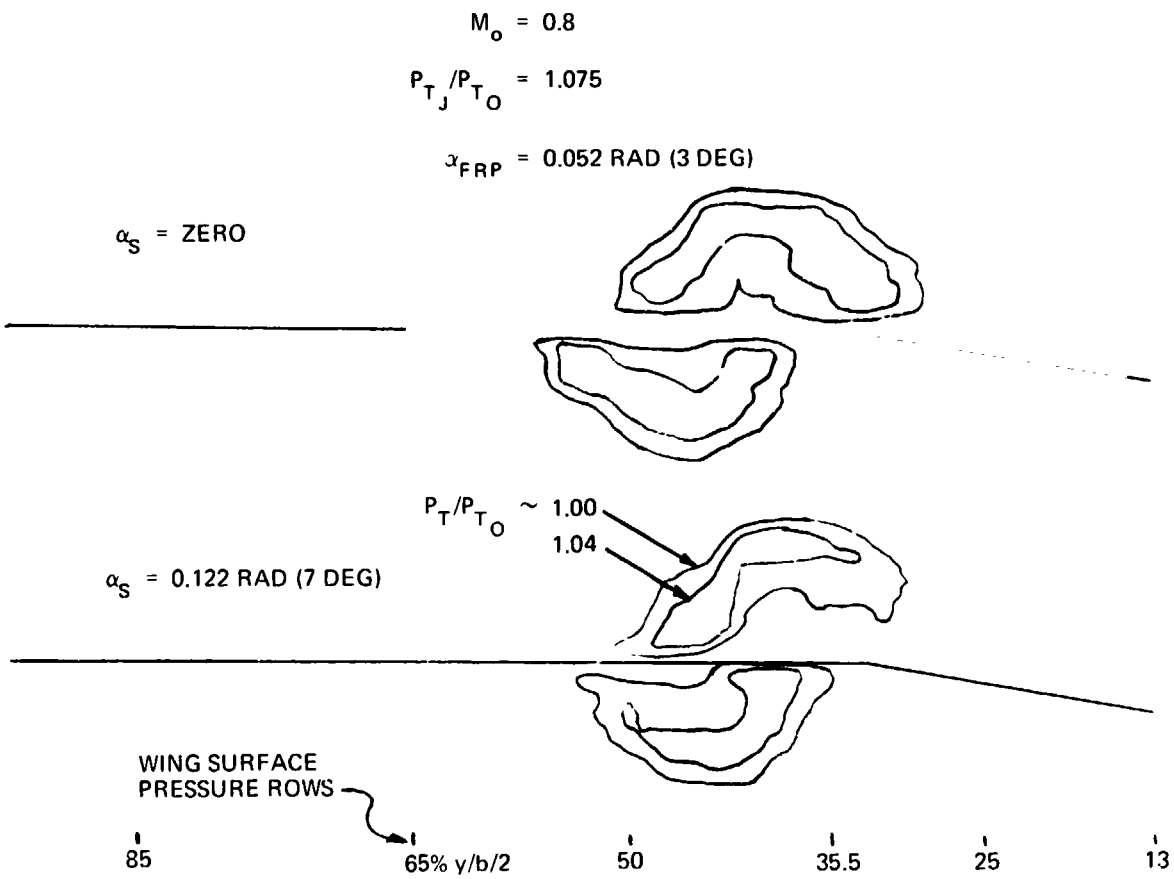

FIGURE 44. EFFECT OF SWIRL ON JET SHAPE

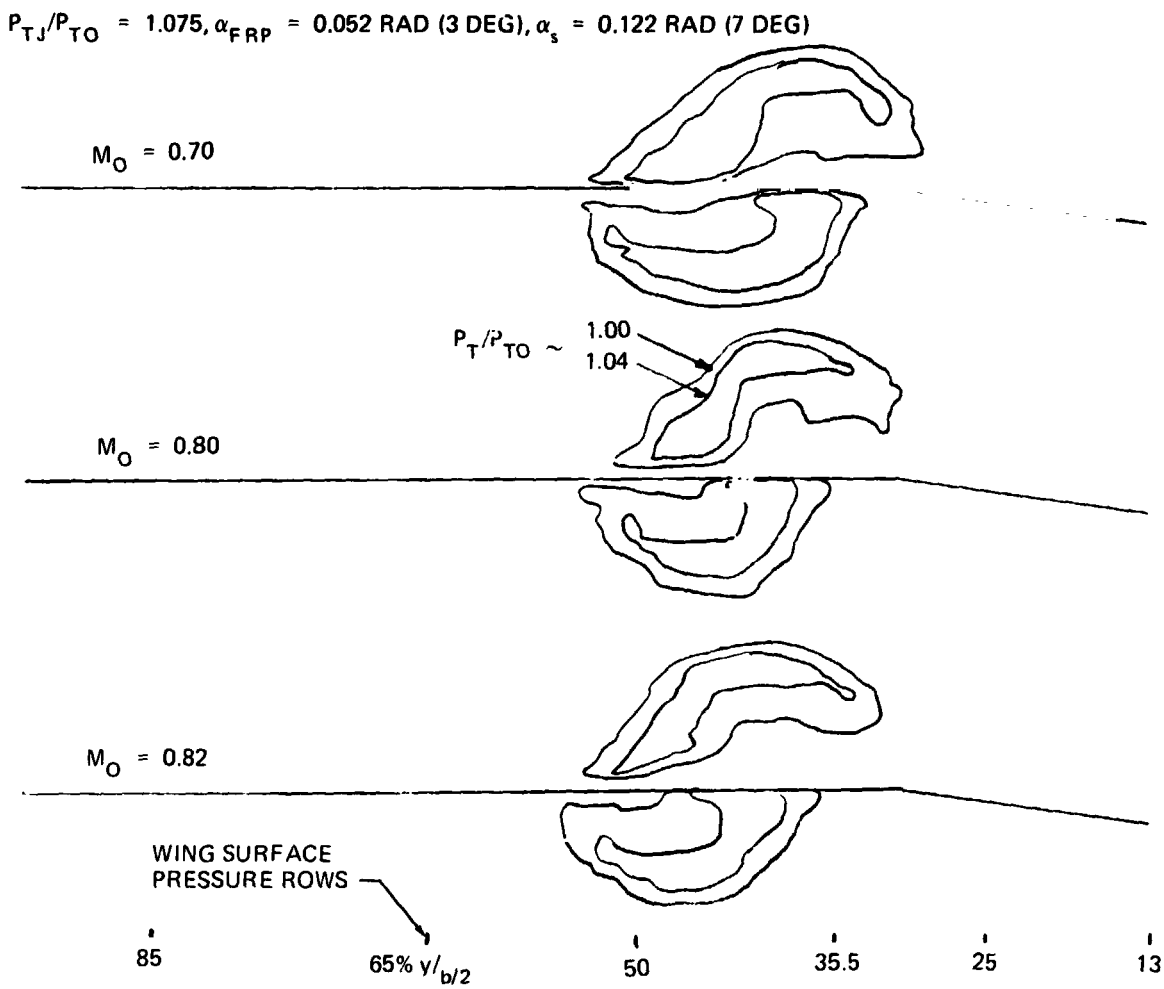

FIGURE 45. EFFECT OF FREE STREAM MACH NUMBER ON JET SHAPE

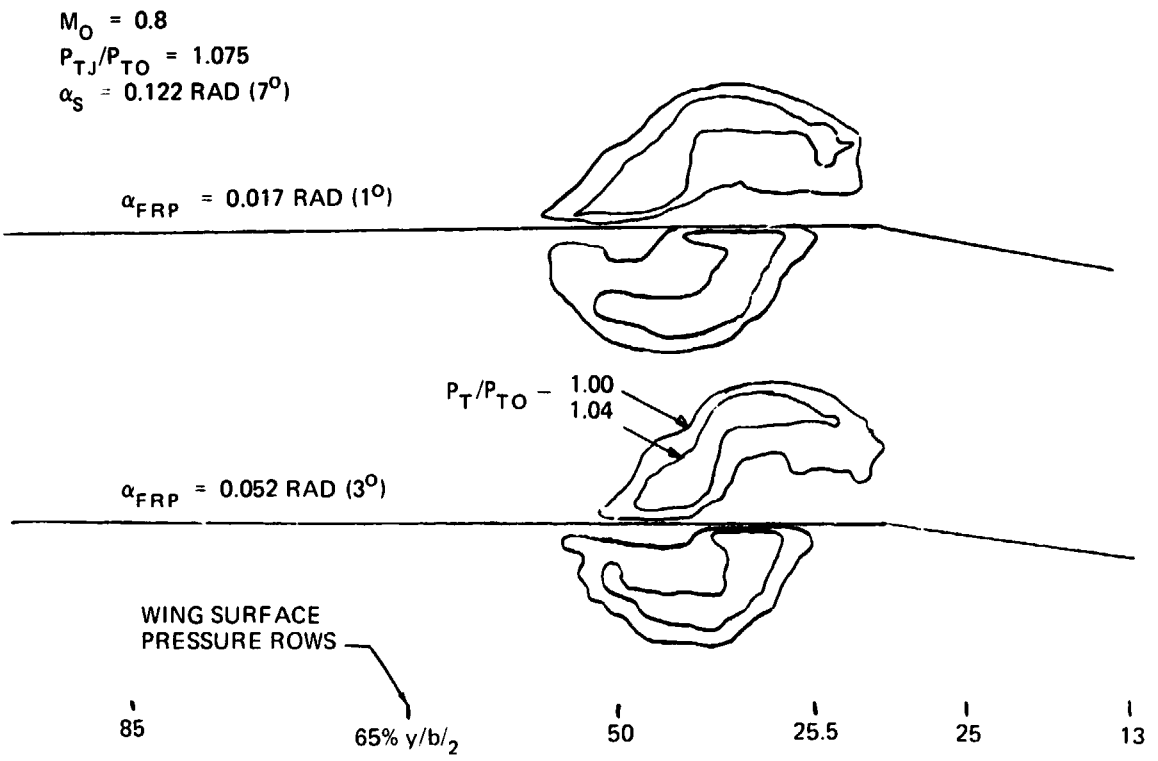

FIGURE 46. EFFECT OF ANGLE OF ATTACK ON JET SHAPE

M_0 = 0.8

α_{FRP} = 0.052 RAD (3^o)

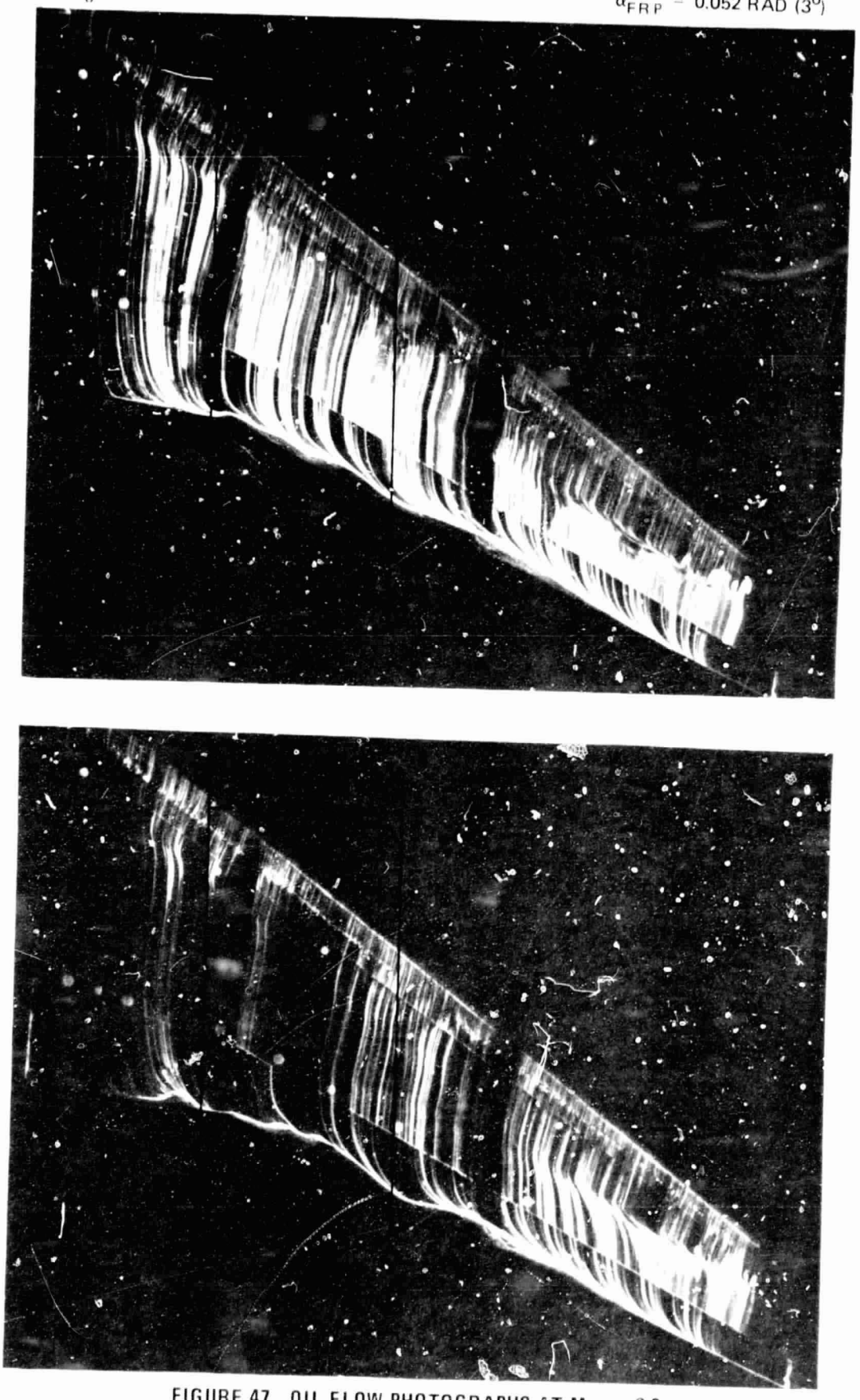

FIGURE 47. OIL FLOW PHOTOGRAPHS AT M_0 = 0.8

M_o = 0.84

α_{FRP} = 0.052 RAD (3^o)

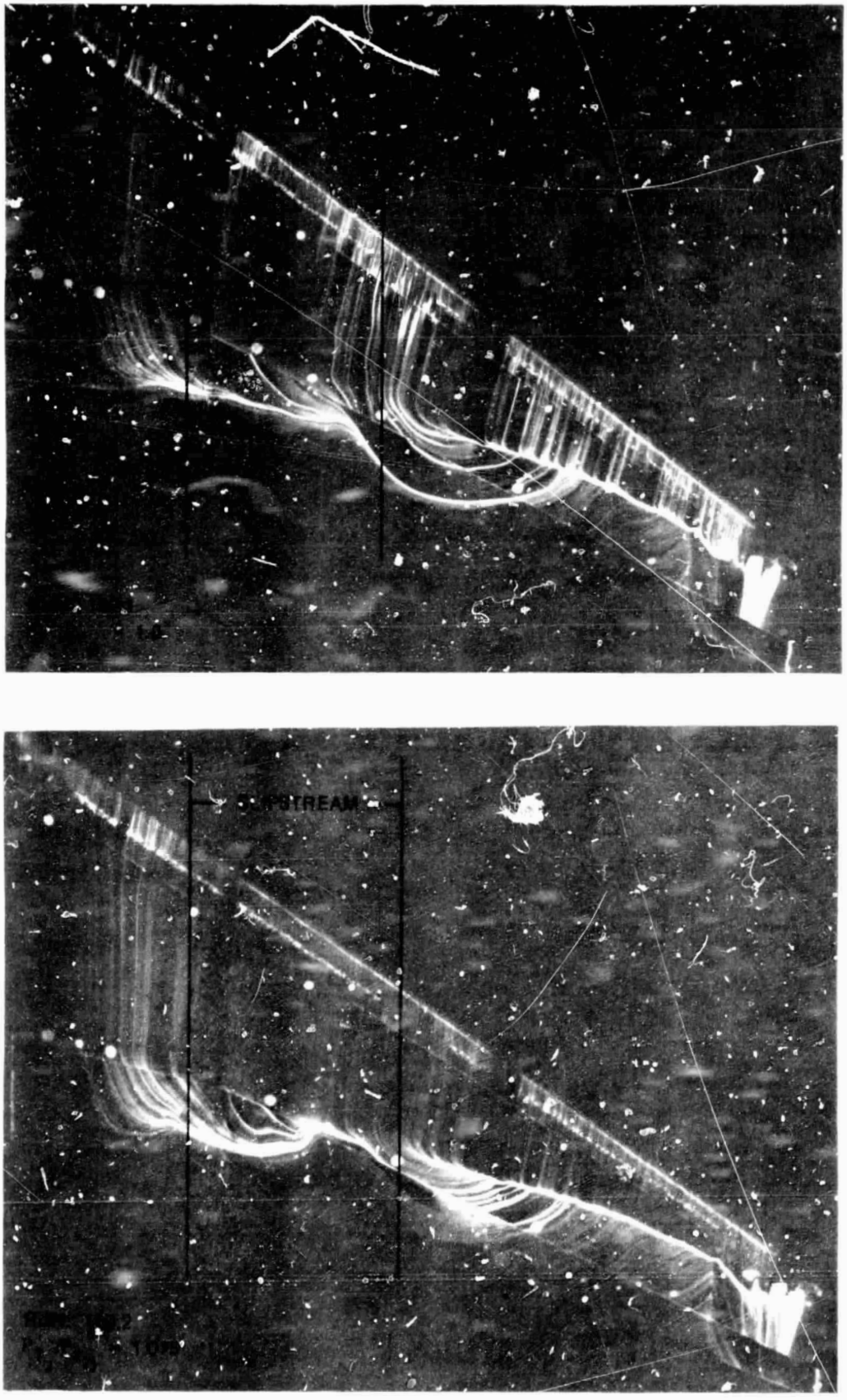

FIGURE 48. OIL FLOW PHOTOGRAPH AT M_0 = 0.84

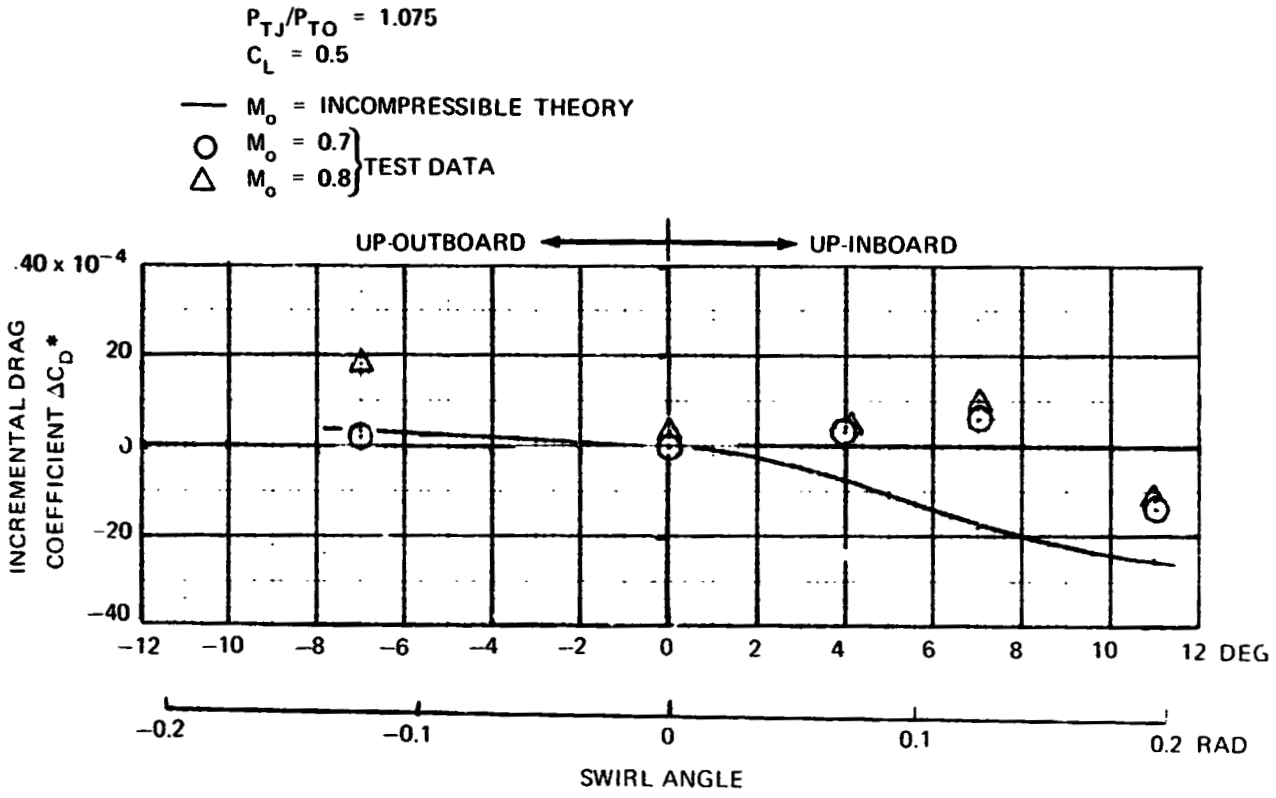

FIGURE 49. COMPARISON OF THEORETICAL AND EXPERIMENTAL INCREMENTAL DRAG DATA

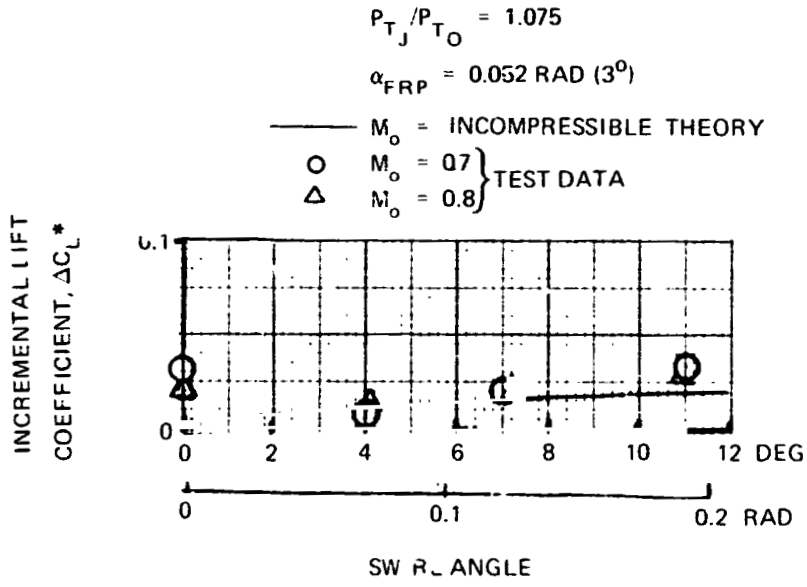

FIGURE 50. COMPARISON OF THEORETICAL AND EXPERIMENTAL INCREMENTAL LIFT DATA

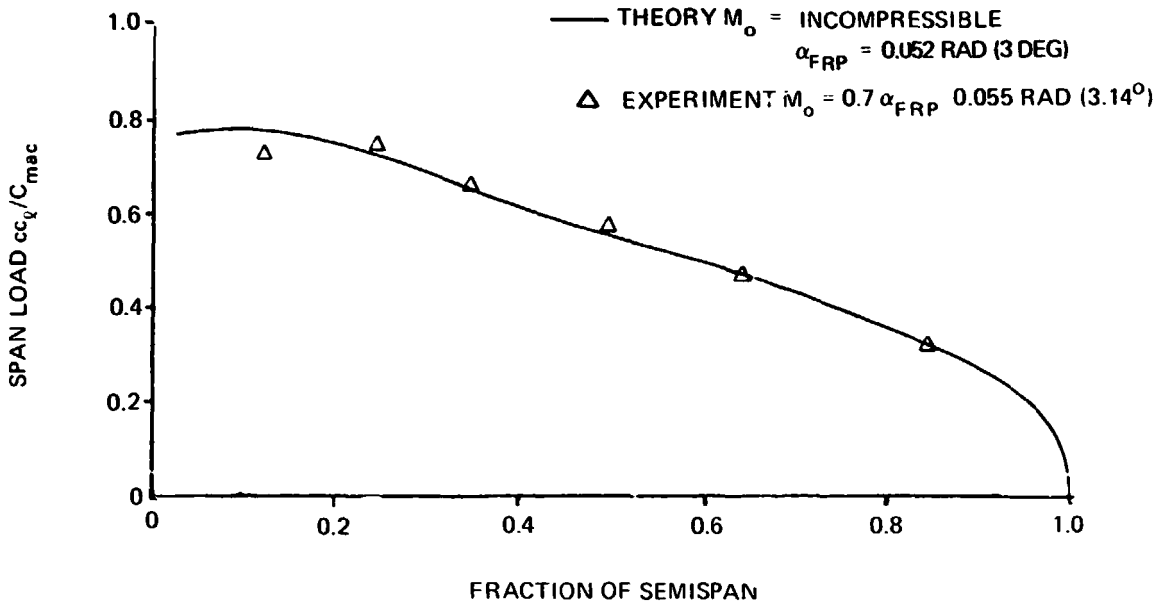

FIGURE 51. COMPARISON OF THEORETICAL AND EXPERMENTAL SPAN LOAD FOR CLEAN WING

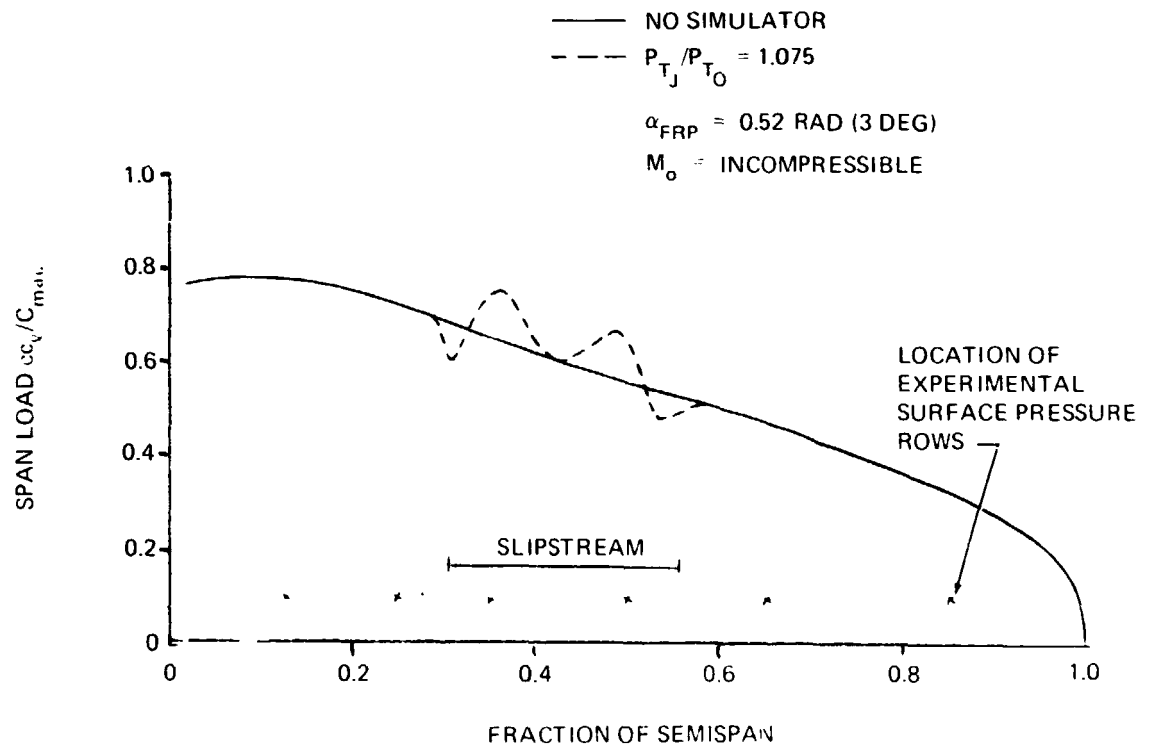

FIGURE 52. THEORETICAL EFFECT OF POWER WITH NO SWIRL ON SPAN LOAD

THEORY	DATA	M_o	CONDITION
———		INCOMP	NO SIMULATOR
– – – –	△	0.7	P_{T_J}/P_{T_O} = 1.075 α_S = 0.122 RAD (+7 DEG) [UP INBOARD]
—·—·—	○	0.7	P_{T_J}/P_{T_O} = 1.075 α_S = −0.122 RAD (−7 DEG) [UP OUTBOARD]

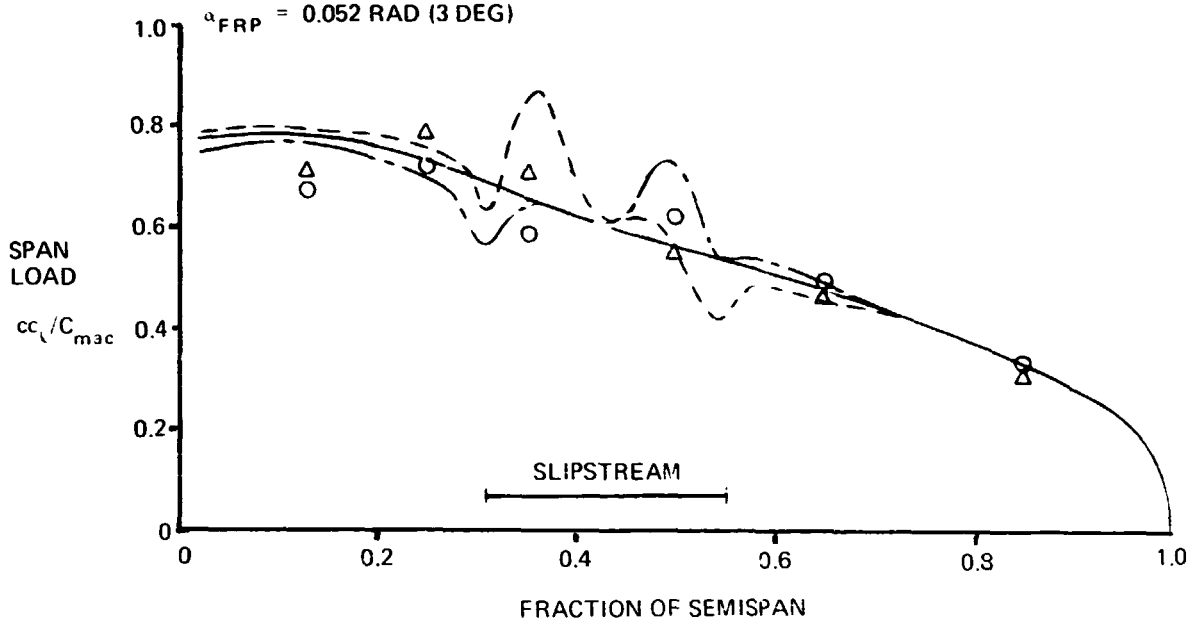

FIGURE 53. EFFECT OF POSITIVE AND NEGATIVE SWIRL ON SPAN LOAD

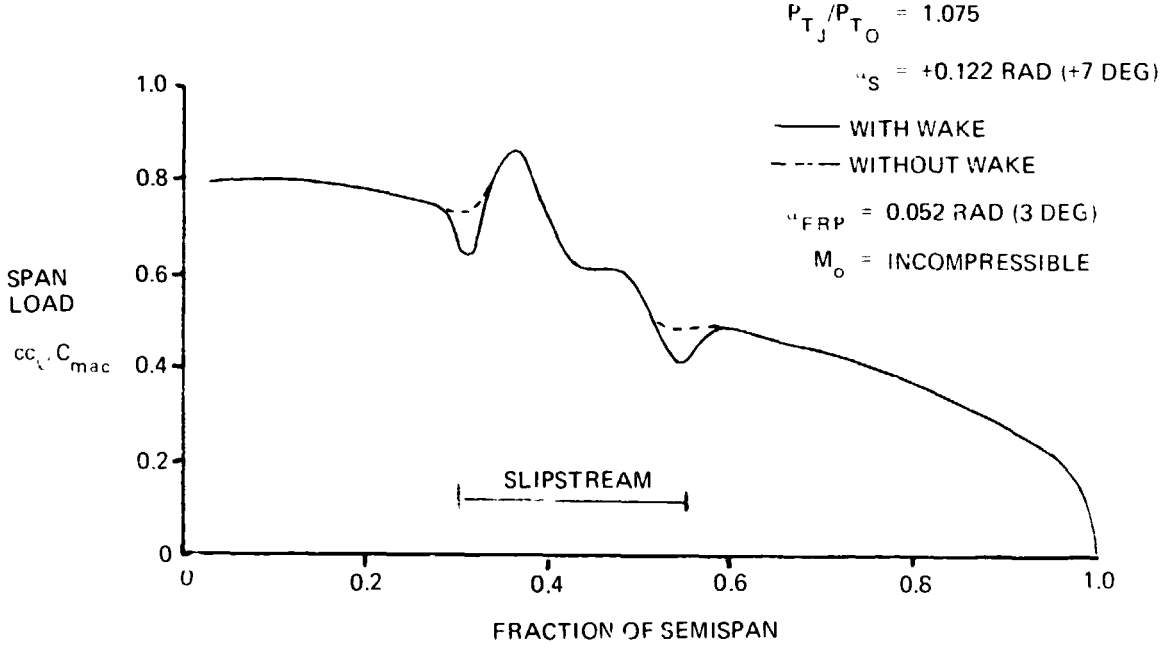

FIGURE 54. THEORETICAL EFFECT OF NACELLE WAKE ON SPAN LOAD